

Star-Forming and Passive Galaxies at $z \sim 2$ in the CFHT Legacy Survey

by

Liz María Arcila Osejo

A Thesis Submitted to

Saint Mary's University, Halifax, Nova Scotia

in Partial Fulfillment of the Requirements for

the Degree of Master of Science in Astronomy

(Department of Astronomy and Physics)

September 30, 2011, Halifax, Nova Scotia

© Liz María Arcila Osejo, 2011

Approved: Dr. Marcin Sawicki (Supervisor)

Approved: Dr. Rob Thacker (Examiner)

Approved: Dr. Luigi Gallo (Examiner)

Date: September 30, 2011.



Library and Archives
Canada

Bibliothèque et
Archives Canada

Published Heritage
Branch

Direction du
Patrimoine de l'édition

395 Wellington Street
Ottawa ON K1A 0N4
Canada

395, rue Wellington
Ottawa ON K1A 0N4
Canada

Your file *Votre référence*
ISBN: 978-0-494-81736-0
Our file *Notre référence*
ISBN: 978-0-494-81736-0

NOTICE:

The author has granted a non-exclusive license allowing Library and Archives Canada to reproduce, publish, archive, preserve, conserve, communicate to the public by telecommunication or on the Internet, loan, distribute and sell theses worldwide, for commercial or non-commercial purposes, in microform, paper, electronic and/or any other formats.

The author retains copyright ownership and moral rights in this thesis. Neither the thesis nor substantial extracts from it may be printed or otherwise reproduced without the author's permission.

AVIS:

L'auteur a accordé une licence non exclusive permettant à la Bibliothèque et Archives Canada de reproduire, publier, archiver, sauvegarder, conserver, transmettre au public par télécommunication ou par l'Internet, prêter, distribuer et vendre des thèses partout dans le monde, à des fins commerciales ou autres, sur support microforme, papier, électronique et/ou autres formats.

L'auteur conserve la propriété du droit d'auteur et des droits moraux qui protègent cette thèse. Ni la thèse ni des extraits substantiels de celle-ci ne doivent être imprimés ou autrement reproduits sans son autorisation.

In compliance with the Canadian Privacy Act some supporting forms may have been removed from this thesis.

Conformément à la loi canadienne sur la protection de la vie privée, quelques formulaires secondaires ont été enlevés de cette thèse.

While these forms may be included in the document page count, their removal does not represent any loss of content from the thesis.

Bien que ces formulaires aient inclus dans la pagination, il n'y aura aucun contenu manquant.


Canada

Acknowledgements

This thesis is based on observations obtained with WIRCam, a joint project of CFHT, Taiwan, Korea, Canada, France, at the Canada-France-Hawaii Telescope (CFHT) which is operated by the National Research Council (NRC) of Canada, the Institut National des Sciences de l'Univers of the Centre National de la Recherche Scientifique of France, and the University of Hawaii. This work is based in part on data products produced at TERAPIX, the WIRDS (WIRcam Deep Survey) consortium, and the Canadian Astronomy Data Centre. This research was supported by a grant from the Agence Nationale de la Recherche ANR-07-BLAN-0228.

In addition, this thesis is based on observations obtained with MegaPrime/MegaCam, a joint project of CFHT and CEA/ DAPNIA, at the Canada-France-Hawaii Telescope (CFHT) which is operated by the National Research Council (NRC) of Canada, the Institut National des Science de l'Univers of the Centre National de la Recherche Scientifique (CNRS) of France, and the University of Hawaii. This work is based in part on data products produced at TERAPIX and the Canadian Astronomy Data Centre as part of the Canada-France-Hawaii Telescope Legacy Survey, a collaborative project of NRC and CNRS. I would like to thank Stephen Gwyn for allowing me to reproduce deep field D1 (CFHT Color) in this project.

I would like to show my gratitude to my supervisor, Dr. Marcin Sawicki for his patience, support, constant encouragement and guidance throughout this project. I would also like to thank Dr. Taro Sato for providing important insight and work in developing this project. I am indebted to everyone at Saint Mary's University whose support has made this research possible, professors, staff and graduate students.

Finally and most importantly I wish to thank my family and friends, specially my mom, Maria Osejo, and my best friend, Paola Pinilla Ortiz. I admire both of you immensely and I am blessed to have you both in my life.

Contents

1	Introduction	1
	Introduction	1
1.1	Background and Motivation	1
1.2	The BzK_s Selection Criteria	3
1.2.1	Galaxy Models	4
1.2.2	The BzK_s Color Selection	7
1.2.3	Morphology and Star Formation Rates	7
1.3	Comparison with other selection criteria	10
2	Data: CFHTLS-WIRDS	11
2.1	Optical Data	12
2.1.1	MegaCam	12
2.1.2	CFHTLS	13
2.2	Infrared Data	14
2.2.1	WIRCam	14
2.2.2	WIRDS	15
2.2.3	Data: The CFHTLS T0006 and WIRDS T0002 releases	16
2.3	Photometry	17
2.4	Selection Criteria	20

2.4.1	Galaxy Models in the BzK_s and gzK_s Diagrams	21
2.4.2	Developing the gzK_s Selection Criteria	26
2.5	ZJHK Selection Criteria	29
3	Results	36
3.1	Galaxy Number Counts	36
3.2	Luminosity Function	49
3.2.1	Effective Volumes	51
3.2.2	Absolute Magnitudes	56
3.2.3	Rest-frame R Luminosity function for the CFHTLS Deep Fields	60
4	Summary, Conclusions and Future Directions.	63
4.1	Future Work	65
	Bibliography	66

List of Figures

1.1	<i>Evolutionary Tracks in the BzK diagram using spectral synthesis models.</i>	5
1.2	<i>Evolutionary Tracks in the BzK diagram using specral synthesis models.</i>	6
1.3	<i>BzK_s Selection Criteria. Figure taken from (Daddi et al. 2004).</i>	8
1.4	<i>z-band imaging from ACS for BzK_s selected galaxies.</i>	9
2.1	<i>CFHTLS Deep Field D1: 1 deg² CFHT color composite. Image by CFHT and Terapix.</i>	12
2.2	<i>MegaCam Filter Set.</i>	14
2.3	<i>Filter transmission Curves for WIRCam broad band filters.</i>	15
2.4	<i>Transmission curves for the original BzK_s Daddi filters and the gzK_s CFHTLS-WIRDS filters. From left to right: blue lines: filters B, z and K_s and red lines: filters g, z and K_s</i>	21
2.5	<i>Bruzual and Charlot (2003) stellar population synthesis models for Constant Star Formation (CSF).</i>	22
2.6	<i>Bruzual and Charlot (2003) stellar population synthesis models for Instantaneous Burst (SSP) Models.</i>	23
2.7	<i>Constant Star Formation Models in the gzK_s color-color plot.</i>	24
2.8	<i>Instantaneous Burst (SSP) Models in the gzK_s color-color plot.</i>	25
2.9	<i>gzK_s comparison with BzK_s Constant Star-Formation Models.</i>	27
2.10	<i>gzK_s comparison with BzK_s instantaneous burst models.</i>	28
2.11	<i>g-band non-detections in SF Galaxies in field D3.</i>	30

2.12	<i>SEDfit color models for $(z-J)$ versus $(H-K_s)$.</i>	31
2.13	<i>$zJHK_s$ star-forming and passive galaxies in D3.</i>	33
2.14	<i>$zJHK_s$ color models for star-forming and passive galaxies.</i>	35
3.1	<i>Galaxy Number counts for all the galaxies in each field.</i>	38
3.2	<i>Galaxy number counts for star-forming galaxies in field D1.</i>	40
3.3	<i>Galaxy number counts for star-forming galaxies in field D2.</i>	41
3.4	<i>Galaxy number counts for star-forming galaxies in field D3.</i>	42
3.5	<i>Galaxy number counts for star-forming galaxies in field D4.</i>	43
3.6	<i>Galaxy number counts for star-forming galaxies selected using their gzK_s colors if they lie below the $(z - K_s) = 2.55$ line and their $zJHK_s$ if they lie above this line.</i>	44
3.7	<i>Galaxy number counts for passive in field D1.</i>	45
3.8	<i>Galaxy number counts for passive galaxies in field D2.</i>	46
3.9	<i>Galaxy number counts for passive galaxies in field D3.</i>	47
3.10	<i>Galaxy number counts for passive galaxies in field D4.</i>	48
3.11	<i>Galaxy number counts for $z \sim 2$ passive galaxies selected using the $zJHK_s$ selection criteria.</i>	49
3.12	<i>Galaxy number counts for $z \sim 2$ star-forming galaxies for our original $zJHK_s$ fit and complementary $zJHK_s$ Fit 2 (See Chapter 2).</i>	50
3.13	<i>Galaxy number counts for $z \sim 2$ passive galaxies for our original $zJHK_s$ fit and complementary $zJHK_s$ Fit 2.</i>	51
3.14	<i>Color gzK_s Models from Bruzual & Charlot (1993) spectral synthesis models for star-forming galaxies.</i>	53
3.15	<i>Conceptual illustration of the probability box $p(z)$.</i>	54
3.16	<i>Effective volume as a function of $E(B-V)$ for different model ages.</i>	55
3.17	<i>Color gzK_s Models from Bruzual & Charlot (1993) spectral synthesis models for passive galaxies.</i>	57

3.18 V_{eff} as a function of age for passive galaxies.	58
3.19 ΔMag as a function of redshift for several different models.	59
3.20 Redshift $z \sim 2$ R band luminosity function for the four Deep fields of the CFHTLS.	61

List of Tables

2.1	<i>Basic filter Characteristics for MegaCam. Data taken from MegaPrime/MegaCam CFH.</i>	13
2.2	<i>Characteristics of WIRCam broad band filters. Information from WIRCam CFHT.</i>	15
2.3	<i>Summary of the properties of the CFHTLS T0006 release for each filter in each field.</i>	17
2.4	<i>Summary of the properties of the WIRDS T0002 release for each filter in each field.</i>	18
2.5	<i>Internal Flags from SExtractor.</i>	19
2.6	<i>Summary of the four Deep Fields.</i>	20
2.7	<i>Comparison between the different population of galaxies found in each field for the gzK_s and $zJHK_s$ color selection.</i>	32
3.1	<i>K_s Magnitude limits and effective areas for the different authors presented to compare our results.</i>	39

Abstract

Star-forming and Passive Galaxies at $z \sim 2$ in the CFHT Legacy Survey.

by Liz María Arcila Osejo

In this work we use the latest results from the four Deep Fields of the Canada France Hawaii Telescope Legacy Survey (CFHTLS) combined with the WIRCam Deep Survey (WIRDS) covering 2.51 deg^2 to study the number counts and luminosity functions of $z \sim 2$ star-forming and passive galaxies to $K_s < 23$. To construct our catalogs, we used an adaptation of the BzK_s selection criteria to the available filters of the CFHTLS: The gzK_s color-color plot combined with a new infrared $zJHK_s$ color selection allows us to discriminate between star-forming and passive galaxies at $z \sim 2$. We build number counts and luminosity functions for these two different populations in each Deep Field and average fields. Our luminosity function for passive galaxies exhibits a flattening and a possible turnover at $K_s \sim 22$. This turnover is clear in some of the Deep fields but not in all of them and this could imply that this turnover is not universal. From this observation, we conclude that the passive galaxy population at $z \sim 2$ is dominated by intermediate-mass objects. Our results are consistent with the downsizing scenario of galaxy evolution in which the most massive systems stop star-formation before less massive ones.

September 30, 2011

Chapter 1

Introduction

1.1 Background and Motivation

The Cold Dark Matter (CDM) theory of structure formation describes the hierarchical structure growth of the dark component in the universe. According to this scenario, smaller systems formed first and then merged into larger structures. Unfortunately, what we observe is the luminous component in galaxies whose relation to the dark component at large scales is relatively simple, but becomes complex at small scales due to the effects of baryonic physics.

One of the main challenges in observational cosmology is trying to understand the formation and evolution of galaxies based on their dark and baryonic component, specifically to test theoretical models of galaxy formation at every redshift. A large number of surveys have been developed during the last decade to construct multiwavelength observations of galaxies using diverse ground and space-based facilities.

One of the main objectives of these surveys is trying to understand how the galaxy populations at early times evolve into those in our local universe. One important feature is how the local most-massive galaxies assembled most of their mass and what type of evolution characterized this growth. A critical epoch for galaxy formation is $2 \leq z \leq 4$ when star-formation activity in the universe was at its peak, and most of the structures in the local universe that we observe were not

present. A specific evolutionary path of the evolution from this redshift to the present time is still undetermined (Shapley 2011, McCracken et al. 2010).

Building large statistical samples of galaxies allows us to explore and understand these important issues at earlier epochs, and helps to develop a more complete view of the evolution of structure in our universe. Large infra-red samples are essential not only because spectral features at these important redshifts move out of the optical into the near-IR, but because they correspond more closely to a star-mass selected sample. This is due to the fact that the flux at these wavelengths comes from relatively less massive, old, cooler stars that represent most of the mass of the system, but also because they are less affected by dust extinction.

A complete exploration of galaxies at these epochs would require large spectroscopic IR surveys, which is time consuming. Consequently, several techniques have been developed based on color-color cuts which are relatively easy to construct due to the fact that they usually only require three or four photometric bands, and can build a sample of galaxies based on whether they are passive or star-forming, a feature that can provide useful information when trying to understand the evolutionary process of these populations.

Some examples of such color-color cuts to select high-redshift galaxies are the Lyman Break Galaxies (Steidel et al. 1996, 2003), Extremely Red Objects (Elston et al. 1998, Thompson et al. 1999, Roche et al. 2002), Distant Red Galaxies (Franx et al. 2003) and the BzK_s Selection Criteria (Daddi et al. 2004). The Lyman Break Technique was developed to select $z \sim 3$ star forming galaxies, missing passively evolving ones and dust reddened star-forming galaxies. The Extremely Red Objects (EROs) and Distant Red Galaxies (DRG) techniques are designed to select passive high-redshift galaxies based on their red colors. However, spectroscopic follow up shows that these samples include both passive galaxies and dust-reddened star-forming galaxies (Cimatti et al. 2002, van Dokkum et al. 2004).

Of all of these techniques, the so called BzK_s selection criteria is the only one able to select and distinguish between star-forming and passive galaxies at $z \sim 2$ (Daddi et al. 2004, Grazian et

al. 2007) (See Section 1.2 for details). This ability provides a way to trace the evolution of these different populations providing a more complete information on galaxy formation and evolution. Combining the BzK_s selection criteria with the large effective areas, ($0.4-1 \text{ deg}^2$) and independent lines of sight of the Canada France Hawaii Telescope Legacy Survey four Deep Fields, we aim in this work to recover and construct a representative statistical sample of star-forming and passive galaxies at these redshifts. Moreover, we aim to construct a rest-frame R luminosity function which allow us to see how many galaxies were already assembled at $z \sim 2$, allowing us to test galaxy formation scenarios.

In Chapter 1, we describe the basics of the BzK_s selection technique and its comparison with other color-color cuts to select high-redshift galaxies. In Chapter 2 we explain the characteristics of our data, how we obtained our photometry and how we adjusted the BzK_s selection criteria to a new gzK_s criteria to match the available filters in our data, and how we developed a second selection criterion, $zJHK_s$, to address ambiguity in our samples due to limiting g-band magnitudes. In Chapter 3 we present galaxy number counts and luminosity functions for star-forming and passive galaxies in our four Deep Fields and compare them with results from other studies based on the BzK_s selection criteria. In Chapter 4 we present our conclusions and future work.

Throughout this project, we use a flat lambda cosmology ($\Omega_m = 0.3$, $\Omega_\Lambda = 0.7$) with $h = H_0/100 \text{ km s}^{-1} \text{ Mpc}^{-1} = 0.7$.

1.2 The BzK_s Selection Criteria

Daddi et al. (2004) introduced a two-color selection criterion aimed at the detection and identification of star-forming and passive galaxies at redshifts $1.4 < z < 2.5$ based on their $(z-K_s)$ versus $(B-z)$ colors.

1.2.1 Galaxy Models

Using Bruzual and Charlot (2003) stellar population synthesis models for constant star-formation and instantaneous burst models, Daddi et al. (2004) considered galaxy evolution in the $(z-K_s)$ versus $(B-z)$ diagram to understand the physical meaning and evolution of BzK_s colors of galaxies in their diagram. Figures 1.1 and 1.2 show the reproduction of the $(z-K_s)$ versus $(B-z)$ colors of stellar population synthesis models for constant star formation and instantaneous burst models from Daddi et al. (2004).

Figure 1.1 shows BzK_s colors of models with solar metallicity and constant star formation (CSF) with ages between 10^{-3} and 2 Gyr, redshifts between $1.4 < z < 2.5$, and different values of reddening using the Calzetti et al. (2000) extinction law. Star-forming galaxies occupy the region left of the diagonal line. These models' $(B-z)$ color does not change much with age, while their $(z-K_s)$ color does increase with age, due to the development of the 4000\AA /Balmer break beyond the z filter. On the other hand, dust affects the $(B-z)$ and $(z-K_s)$ colors by the same amount, since the change in the colors will be due to dust extinction and not a break in the spectra. The reddening vector lies parallel to the diagonal line.

To represent passively evolving galaxies in Figure 1.2, Daddi et. al (2004) used solar metallicity and instantaneous burst models, with ages between 0.1 and 2 Gyr, and no reddening. Models with young ages (0.1 and 0.2 Gyr) will still be selected as star-forming galaxies but as they get older, the evolutionary tracks start to occupy the region to the right and above the horizontal line. As can be seen in Figure 1.2, models with ages of 0.5 Gyr would be missed by this criterion. Nevertheless, Daddi et al. (2004) argue that such young stellar populations with single stellar population (SSP) models and no reddening are possibly an unrealistic model for passive galaxies, since at this age these models are still probably star-forming galaxies with some amount of reddening. Due to the fact that the reddening vector lies parallel to the diagonal line it is possible to distinguish between dusty star-forming galaxies which evolve parallel to the diagonal line and truly passive ones that lie to the right of the diagonal line and above the horizontal one.

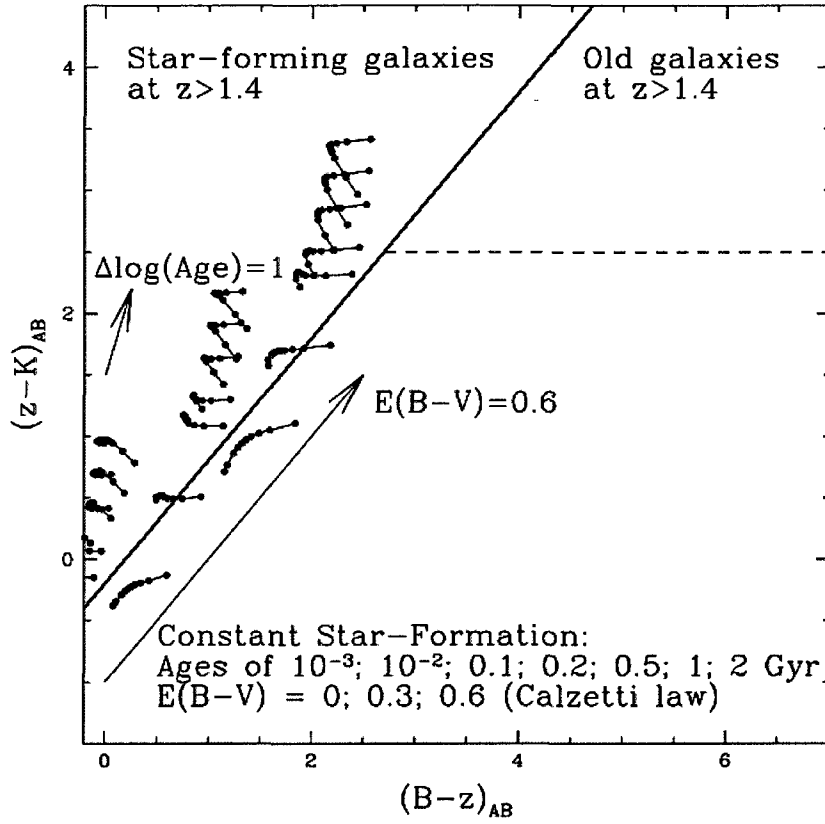


Figure 1.1: *Evolutionary Tracks in the BzK diagram using spectral synthesis models. Different tracks represent different models with constant star formation, for ages between 1 Myr and 2 Gyr, and $E(B-V)=0, 0.3$ and 0.6 . Every point in each track represents the evolution in redshift between $1.4 < z < 2.5$. Also represented in the image are the evolutionary trends as age and $E(B-V)$ increase. Figure taken from Daddi et al. (2004). Reproduced by permission of the AAS.*

Based on these clearly defined regions, a selection criterion was developed to distinguish between star-forming and passive galaxies. Star-forming galaxies are selected using the criterion defined in Equation 1.1:

$$BzK \equiv (z - K)_{AB} - (B - z)_{AB} \geq -0.2 \text{ Star Forming Galaxies.} \quad (1.1)$$

Passive galaxies are selected using Equation 1.2 and stars are distinguished using the color criteria in Equation 1.3

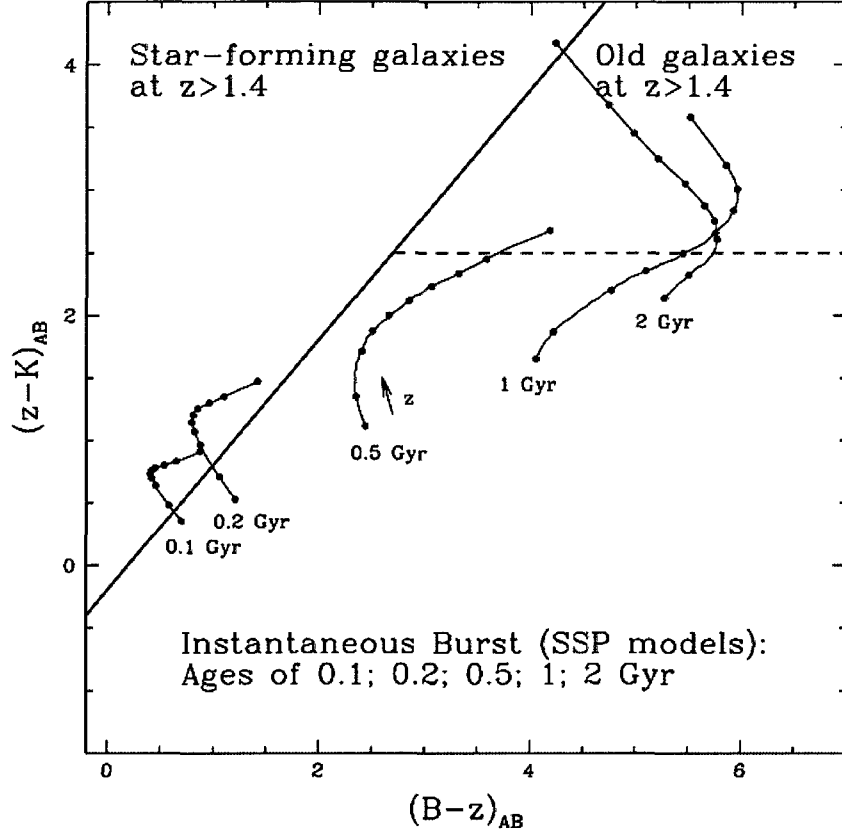


Figure 1.2: *Evolutionary Tracks in the BzK diagram using spectral synthesis models. As in Figure 1.1, different tracks represent different models but this plot reproduces Instantaneous Burst Models, for ages between 0.1 and 2 Gyr and no reddening. Every model in the diagram has a label according to its age. The small arrow in the 0.5 Gyr model represents the redshift evolution in each model between $1.4 < z < 2.5$. Figure taken from Daddi et al. (2004). Reproduced by permission of the AAS.*

$$BzK < -0.2 \text{ AND } (z - K)_{AB} > 2.5 \text{ Passive Galaxies.} \quad (1.2)$$

$$(z - K)_{AB} < 0.3(B - z)_{AB} - 0.5 \text{ Stars.} \quad (1.3)$$

1.2.2 The BzK_s Color Selection

Figure 1.3 shows the $(B-z)$ versus $(z-K_s)$ diagram known as the BzK_s color selection from the K20/GOODS sample (Daddi et al. 2004). The K20 survey obtained spectra of 545 objects over two separate fields (one of them the GOODS- South Field). At $K_{Vega} < 20$, 328 of the 347 objects in this area have been spectroscopically identified. Besides spectroscopy, photometry and imaging are available for this field.

Based on spectroscopic results in the K20 survey, and as expected from their stellar population modeling, Daddi et al. (2004) determined that star-forming galaxies and passive galaxies lie in different loci of this diagram. As shown in Figure 1.3 every galaxy that lies to the left of the diagonal line, represents a star-forming galaxy, while everything to the right of the diagonal line and above the horizontal one represents a passive galaxy. Stars are also clearly identified to lie below the dotted diagonal line.

Identification of star-forming galaxies in the BzK_s plot in Figure 1.3 relies in the detection of $[OII] \lambda 3727$ for galaxies at $1.4 < z < 1.7$ while star-forming galaxies at $z > 1.7$ are identified by some other features such as CIV absorption at 1550\AA . Passive galaxies are identified by the detection of continuum breaks and absorption features in their rest-frame $2500\text{-}3000\text{\AA}$ region. (Cimatti et al. 2004).

1.2.3 Morphology and Star Formation Rates

To further elucidate the validity of the BzK_s selection criteria, Daddi et al. (2004) used imaging from ACS (Advanced Camera for Surveys at HST) to obtain morphological information on these color-selected galaxies. Figure 1.4 shows z-band imaging of 32 galaxies that were selected using the BzK_s criteria. According to their colors they have been labeled “S” for star-forming and “P” for passive galaxies.

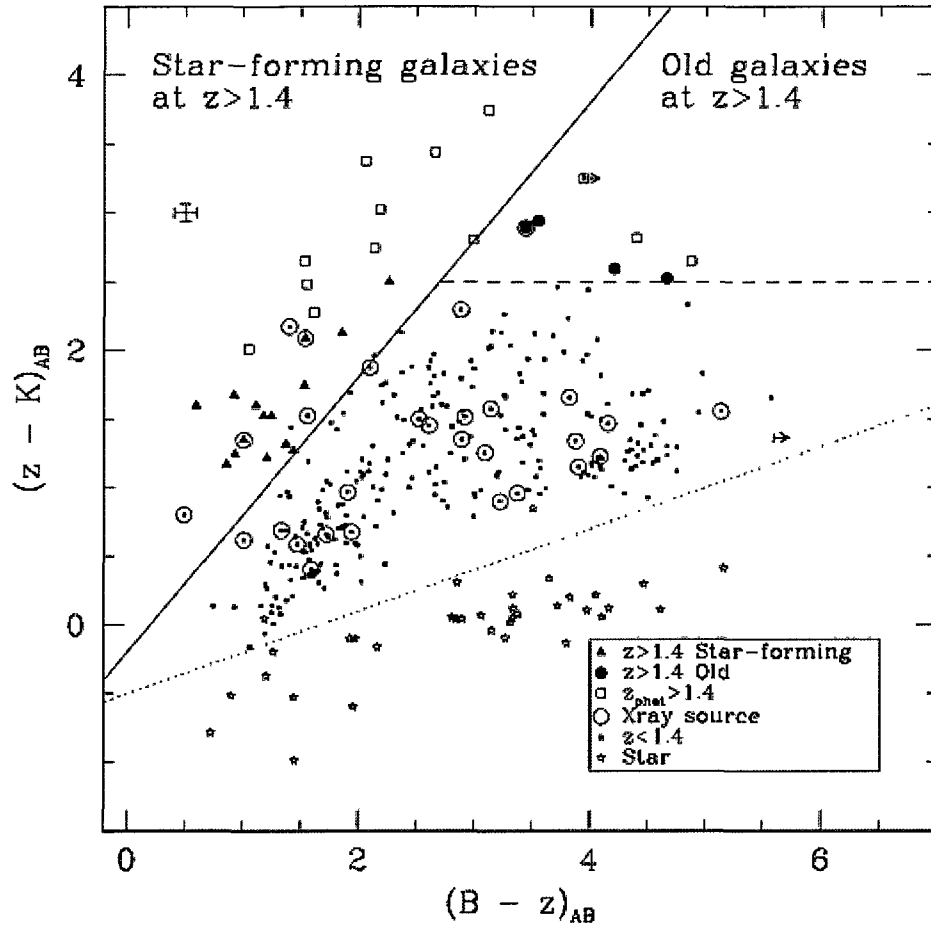


Figure 1.3: BzK_s Selection Criteria. Figure taken from (Daddi et al. 2004). Solid triangles represent objects with spectral features typical of star-forming galaxies and spectroscopic $z > 1.4$. Solid circles are $z > 1.4$ galaxies with old stellar populations as determined from spectroscopy. Open squares are objects with $z_{phot} > 1.4$ and no spectroscopic redshift available. Open circles represent X-ray sources from Giacconi et al. (2002) and/or Alexander et al. (2003). Solid lines define the regions used to isolate star-forming and passive galaxies at $z \sim 2$. Reproduced by permission of the AAS.

As can be seen, objects identified as star-forming ($BzK \geq -0.2$) appear to be large irregular or merging systems while passive galaxies ($BzK < -0.2$ AND $(z - K) > 2.55$) have a more compact morphology.

In Daddi et al. (2004) star-formation rates (SFR) were determined for those galaxies photometrically

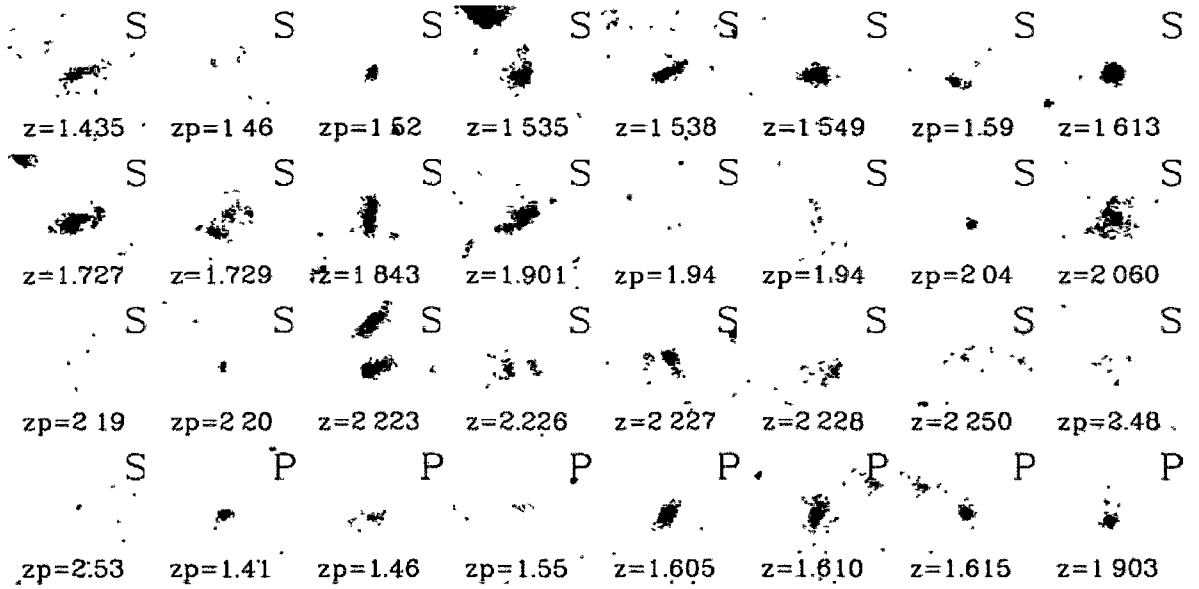


Figure 1.4: z -band imaging from ACS for BzK_s selected galaxies. Galaxies are labeled either as “S” (Star-forming) or “P” (Passive) according to their classification based on their BzK_s colors, each figure also contains information of their spectroscopic (z) or photometric (z_p) redshift. Galaxies classified as star-forming (S) are in general irregulars with very large sizes while passive galaxies (P) are in general compact and with a regular morphology. Figure taken from Daddi et al. (2004). Reproduced by permission of the AAS.

classified as star-forming, based on their BzK_s colors using spectral energy distributions (SED), X-ray luminosities and radio luminosities. Overall, from their full observed spectral energy distributions, typical SFRs for star-forming BzK_s lie between $100\text{-}600 M_{\odot}\text{yr}^{-1}$, while for X-rays luminosities the average SFR is of the order of $\sim 190 M_{\odot}\text{yr}^{-1}$ and, from radio luminosities they obtained an average SFR of $\sim 270 M_{\odot}\text{yr}^{-1}$. On the other hand, X-ray observations of BzK_s galaxies from Reddy et al. (2005) give an average SFR for passive galaxies of $\sim 28 M_{\odot}\text{yr}^{-1}$.

From these results, it can be seen that star-formation rates and morphologies are consistent with what is expected for star forming and passive galaxies.

1.3 Comparison with other selection criteria

Several selection criteria have been developed to select high-redshift galaxies based on their colors. Some of the most notable examples are Lyman Break Galaxies (LBGs), Extremely Red Objects (EROs), Distant Red Galaxies (DRGs) and the BzK_s selection technique. However, only the BzK_s selection technique has the ability to select and distinguish star-forming and passive galaxies at high redshift.

The Lyman Break Technique (Steidel et al. 1996, 2003) was developed to detect star-forming galaxies based on their rest-frame UV colors at $z \sim 3$. This method requires that the UV continuum is relatively flat which limits the selection to star-forming and relatively dust-free galaxies. Although this technique has been extended to select galaxies at a redshift range that fully matches the BzK_s criteria (Steidel et al. 2004), it misses two important populations of high-redshift galaxies, namely passively evolving ones and actively star-forming galaxies that are heavily reddened by dust.

Colors can also be used to detect high-redshift passively evolving galaxies, one example of such a method are Extremely Red Objects (EROs) (Elston et al. 1998 Thompson et al. 1999, Roche et al. 2002), which selects red galaxies at $z \sim 1$ based on their optical to near-infrared colors $(R-K) > 5$. Nevertheless spectroscopy of EROs shows that these objects contain both old passively evolving galaxies and dusty star-forming galaxies (Cimatti et al. 2002).

Developed to identify old stellar systems up to $z \leq 4$, Distant Red Galaxies (DRG) was developed by Franx et al. (2003) using the criterion: $(J-K)_{VEGA} > 2.3$. This selection is similar to EROs $(R-K) > 5$ and will result in selecting both passively evolving and reddened star-forming galaxies (Reddy et al. 2005).

Based on all of these constraints in selecting high-redshift galaxies, it is apparent that none of these criteria have the ability to select and distinguish between star-forming and passive galaxies at $z \sim 2$. This is why the BzK_s selection criteria is important at providing representative and well separated samples of star-forming and passive galaxies at $z \sim 2$

Chapter 2

Data: CFHTLS-WIRDS

The Canada France Hawaii Telescope Legacy Survey (CFHTLS), is a large project developed by Canada and France during five years which combines 50% of dark and grey telescope time. The CFHTLS consists of three different surveys from the Solar System to the distant universe: The Very Wide Survey, covers a total area of 410 square degrees and its purpose is to provide a sample of the solar system population beyond Neptune. The Wide Survey, a wide synoptic survey, covers 170 square degrees and its purpose is to study matter distribution, large scale structures, and clusters of galaxies through weak lensing, morphology and photometric properties of galaxies. Finally, the Deep Survey, which is the survey that we are using for this project, was developed to detect 500 type Ia Supernovae and to study galaxy distribution down to a limiting magnitude $r'=28$. Its main purpose was to lead to a better understanding of the early universe.

The survey area of the Deep Survey is spread over four different fields, D1, D2, D3 and D4. These fields were selected such that they will fulfill certain constraints, *i.e.*, low dust extinction and right ascension distribution over the year. Figure 2.1 shows CFHTLS Deep Field 1¹, as seen by MegaCam (Section 2.1). Four independent fields represent four independent lines of sight which

¹The MegaPipe CFHTLS pages D1,
<http://www3.cadc-ccda.hia-ihp.nrc-cnrc.gc.ca/community/CFHTLS-SG/docs/cfhtlsD1.html>

allows us to monitor the effects of cosmic variance.



Figure 2.1: *CFHTLS Deep Field D1: 1 deg² CFHT color composite. Image by CFHT and Terapix.*

2.1 Optical Data

2.1.1 MegaCam

MegaCam is the wide-field imager at MegaPrime, the wide field optical facility at CFHT. It consists of 36, 2048 x 4612 pixel (340 Megapixels) CCDs covering a 1degree per 1 degree field-of-view with a resolution of 0.186 arcsecond per pixel.

MegaPrime has five broad band filters (u^* , g' , r' , i' , z') which were designed to match the Sloan Digital Sky Survey (SDSS) as closely as possible except for u^* . Mauna Kea (where CFHT is located) has less UV extinction than the SDSS Apache Point site, and consequently the u^* filter is designed to take advantage of this fact.

Filter	u*	g'	r'	i'	z'
Central wavelength [nm]	374	487	625	770	n/a
Wavelength range [nm] at 50%	337-411	414-559	564-685	698-843	823-...
Bandwidth [nm]	74	145	121	145	n/a
Mean Transmission (%)	69.7	84.6	81.4	89.4	90.2

Table 2.1: *Basic filter Characteristics for MegaCam. Data taken from MegaPrime/MegaCam CFH.*

Table 2.1 gives basic filter characteristics² and Figure 2.2 shows the MegaCam transmission and response curves for the filter set. Dashed lines represent filter transmission curves while solid lines represent the total throughput of the system, once the filter transmissions have been multiplied by the instrumental response (mirror+optics+CCD).

2.1.2 CFHTLS

The Canada France Hawaii Telescope Legacy Survey, CFHTLS, comprises observations made with MegaCam for the four Deep Fields in six filters: u*, g', r', i', y' and z'. The latest release, T0006 contains data from two different i filters: the original i filter and a new i filter, called y (or i_2) which was installed in October of 2007 after the original i filter broke. The transmission curves between these two filters are slightly different, and as a result, it was decided to keep both sets of data for these two i filters separate and name them differently.

T0006 has two sets of data, one with the 85% best-seeing images, and the other with the 25% best-seeing images. These images cover a field of view of 1deg^2 for each field with a pixel scale of $0.186''$.

²Technical considerations to prepared MegaCam observations
MegaPrime/MegaCam CFH, <http://www.cfht.hawaii.edu/Instruments/Imaging/MegaPrime/specsinformation.html>

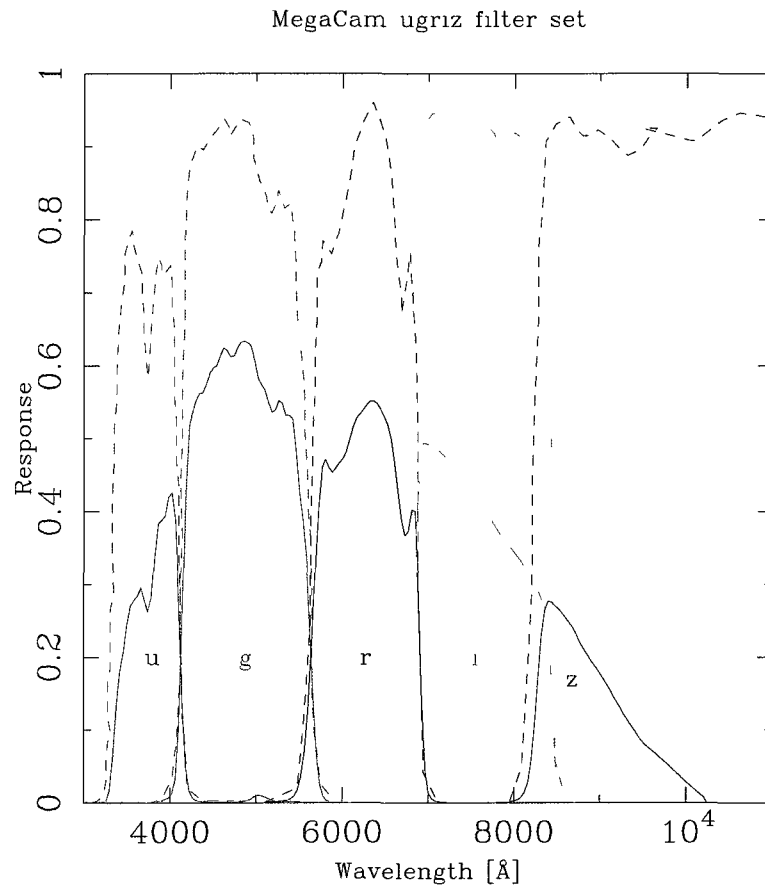


Figure 2.2: *MegaCam Filter Set.* Dashed lines represent transmission curves while solid lines represent the total response of the system once the the filter transmission has been multiplied by the telescope response.

2.2 Infrared Data

2.2.1 WIRCam

WIRCam or Wide-field InfraRed Camera is the near-Infrared wide-field imager at CFHT. WIRCam consists of four detectors in a 2x2 array with 2048 x 2048 active pixels which covers 20 arcmin x 20 arcmin field-of-view with a sampling of 0.3 arcsec per pixel. It has four broad-band filters, Y, J, H, K_s (filter transmission curves shown in Figure 2.3³) and seven narrow-band filters. Table 2.2 shows

³WIRCam Filters, CFHTLS, <http://www.cfht.hawaii.edu/Instruments/Filters/wircam.html>

some model values for the WIRCam broad-band filters⁴:

Filter	Central Wavelength (nm)	Bandwidth (nm)	QE
J	1253	487	0.75
H	1631	289	0.75
K_s	2146	325	0.8
Y	1020	100	0.5??

Table 2.2: Characteristics of WIRCam broad band filters. Information from WIRCam CFHT.

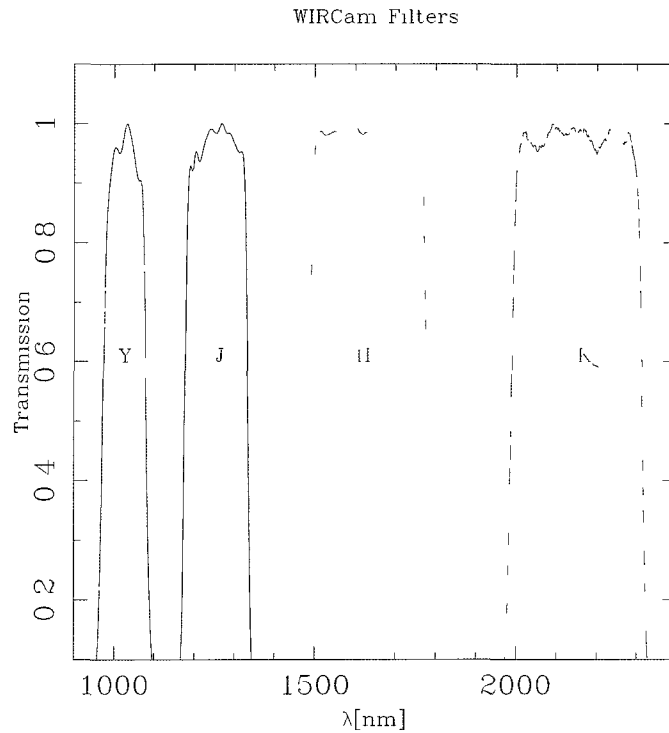


Figure 2.3: Filter transmission Curves for WIRCam broad band filters. Information taken from CFHT, WIRCam Filters.

2.2.2 WIRDS

The WIRCam Deep Survey, or WIRDS (Bielby et al. in prep.) is a large project carried out at CFHT between 2006 and 2008 to obtain near infrared, broad band photometry of the four Deep fields from the CFHTLS.

⁴WIRCam Throughput. WIRCam CFH, <http://www.cfht.hawaii.edu/Instruments/Imaging/WIRCam/WIRCamThroughput.html>

The resulting images contain data from the J , H , and K_s filters that have been re-sampled to match the 0.186 arcsec/pixel MegaCam pixel scale, to ensure that each pixel in the WIRDS images will match the same location in the optical CFHTLS T0006 images. Nevertheless, WIRCam has a smaller field of view than MegaCam and since our photometry is based on K_s selection, most of the effective areas will be smaller than the original 1deg^2 of MegaCam (see Table 2.5). Deep Field 2 is an exception since the full one square degree field has been observed with WIRCam and its J-band image was taken with the WFCAM instrument on UKIRT.

2.2.3 Data: The CFHTLS T0006 and WIRDS T0002 releases

Our data is comprised of combined results from the T0002 release from WIRDS and the T0006 release from CFHTLS. There are several entities involved in the data acquisition and processing: CFHT was used for data acquisition and calibration. Pre-processing of the images was done by Terapix⁵. Pre-processing involves image quality checking; flat fielding; stacking from dithering; identification of bad pixels; and removal of cosmic rays and saturated pixels; background estimation; and astrometric and photometric calibration. Finally, The Canadian Astronomy Data Centre (CADC) is involved in archiving and providing the data products to the community. The processed images consists of the 25% best-seeing stacked images from CFHTLS and the 85% best-seeing stacked images from WIRDS. These were the images retrieved for this project.

A summary of the properties for each filter in each field is given by Tables 2.3 and 2.4. ^{6 7}

⁵Traitement Élémentaire Réduction et Analyse des PIXels, Institut d'Astrophysique de Paris, <http://terapix.iap.fr/>

⁶The CFHTLS T0006 Release, Y. Goranova et al. 2009

⁷WIRDS-T0002 data overview. Terapix, terapix.iap.fr/rubrique.php?id_rubrique=261 2009

Field	Parameter	u*	g	r	i	y	z
D1	<i>Exposure Time [s]</i>	22443	27233	50411	79052	27724	58331
D1	<i>Compl. 80% ext. (AB)</i>	25.52	25.29	24.68	24.32	24.28	23.83
D1	<i>Seeing ["]</i>	0.74	0.68	0.64	0.63	0.58	0.58
D2	<i>Exposure Time [s]</i>	~25000	30834	50893	89404	51008	52930
D2	<i>Compl. 80% ext. (AB)</i>	25.64	25.30	24.68	24.38	24.39	23.90
D2	<i>Seeing ["]</i>	0.75	0.69	0.63	0.61	0.63	0.57
D3	<i>Exposure Time [s]</i>	21787	23419	42027	73870	28053	42142
D3	<i>Compl. 80% ext. (AB)</i>	25.45	25.29	24.69	24.39	24.36	23.71
D3	<i>Seeing ["]</i>	0.76	0.68	0.65	0.63	0.64	0.54
D4	<i>Exposure Time [s]</i>	23103	27862	46448	73330	19883	60490
D4	<i>Compl. 80% ext. (AB)</i>	25.37	25.26	24.65	24.31	24.22	23.76
D4	<i>Seeing ["]</i>	0.77	0.71	0.61	0.58	0.60	0.57

Table 2.3: Summary of the properties of the CFHTLS T0006 release for each filter in each field. 80% compl. ext. is the 80% completeness limit for extended objects. Information taken from The CFHTLS T0006 Release.

2.3 Photometry

We used SExtractor (Bertin and Arnouts 1996) for object detection and photometry in our data. SExtractor (Source Extractor) is a software tool used to detect, measure, classify and perform photometry from astronomical images.

SExtractor was used in dual mode, this means that galaxies and photometric apertures were detected in the K_s band, but the photometry was determined from the other available bands. For detection, it was required that an object should have a minimum of 5 pixels above the 1.2σ sky level.

Kron-like apertures, in which the first image moment is used to determine the flux of the galaxy from a circular/elliptical aperture, (Kron, 1998) were used to determine the total magnitude of a galaxy, while a ten-pixel aperture was used to define the color for each object. As its name suggests, a ten-pixel circular aperture determines the magnitude of a galaxy using a ten-pixel aperture around the object, or in our case, the magnitude of the galaxy from a 1.86 arcseconds aperture.

To ensure that the 1.86 arcseconds (10 pixel) color apertures captures the same fraction of a galaxy's flux in each waveband, Dr. Taro Sato performed smoothing on our images before running SExtractor. In this process, he smoothed these images to match the PSF of the image with the

Field	Parameter	K_s	J	H
D1	Exposure Time [s]	15700	12105	13600
D1	50% point source compl. (AB)	24.73	24.94	24.71
D1	Seeing ["]	0.73	0.80	0.68
D2	Exposure Time [s]	*	*	*
D2	50% point source compl. (AB)	24.32	24.25	24.54
D2	Seeing ["]	0.80	1.09	0.86
D3	Exposure Time [s]	17500	16700	15800
D3	50% point source compl. (AB)	24.69	25.00	24.86
D3	Seeing ["]	0.74	0.81	0.72
D4	Exposure Time [s]	14200	17500	14900
D4	50% point source compl. (AB)	24.62	2510	24.62
D4	Seeing ["]	0.71	0.73	0.69

Table 2.4: Summary of the properties of the WIRDS T0002 release for each filter in each field. 50% point source compl. is the 50% completeness limit for point source objects. Information taken from The WIRDS-WIRCAM Second Data Release. * Exposure times for D2 are part of the COSMOS Survey and are not specified in the Terapix WIRDS website.

worst seeing. Colors used in the color-color selection were determined from smoothed images using ten-pixel magnitudes while, as we will see in Chapter 3, galaxy number counts and luminosity functions were determined from the total unsmoothed K_s band magnitude of the galaxy.

To run SExtractor we generated external flags in the original images to determine spurious regions that could give detections that are not likely to be real or whose photometry could be affected by the light of bright stars. Specific examples of these regions are diffraction spikes, satellite trails or reflective halos from bright stars caused by reflections from the CCD surface to the optics and then back to the CCD.

A second set of flags is generated from the weight image of each band. This weight image gives the individual pixels in the detection image a weight. A flag will be assigned to those pixels whose weight is equal to zero (i.e. bad pixels, where there is no exposure signal).

Internal flags given from SExtractor are also available, these are a set of specific numbers from zero to 128. We only considered objects with internal flags less or equal to four for our

number counts and luminosity function. Objects with internal flags less than or equal to four will include objects without major problems and objects whose characteristics will not affect their colors considerably. Selecting objects with internal flags less than or equal to four do not represent a considerable loss of data since objects with internal flags greater than four represent approximately 1.6% of our sample. Table 2.5 gives a description for the definition of these internal flags as given by the SExtractor documentation⁸.

Flag	Meaning
1	The object has neighbours
2	The object was originally blended with another one
4	At least one pixel of the object is saturated (or very close to)
8	The object is truncated (too close to an image boundary)
16	Object's aperture data are incomplete or corrupted
32	Object's isophotal data are incomplete or corrupted
64	A memory overflow occurred during deblending
128	A memory overflow occurred during extraction

Table 2.5: *Internal Flags from SExtractor. For our results we only consider objects with internal flags less or equal to four. Information taken from SExtractor v 2.5 User's Manual.*

Correction by local dust from our galaxy was made based on Schlegel Dust Maps (Schlegel et al. 1998). These maps are based on composite full sky $100\mu m$ maps from COBE and IRAS, with point sources and zodiacal foreground removed. Their purpose is to be an estimate of Galactic extinction. Using these maps, and the center position of our fields, we can determine the color excess ($E(B-V)$) for each field: See Table 2.6. We then used tables of $E(B-V)$ to extinction in common broadband filters to determine the correction applied for each filter.

Using these results, we created combined catalogs from all the bands (u^* , g' , r' , i' , z' , J, H, K_s), including magnitudes from Kron-like apertures, ten-pixel apertures, their corresponding uncertainties, fluxes, internal and external flags.

Table 2.6 gives a summary of the four Deep fields, specifically the resulting effective area after taking into account regions removed from the external flags, and a summary of the objects found.

⁸SExtractor v2.5 User's Manual, E. Bertin, Institut d'Astrophysique and Observatoire de Paris

Columns labeled as SF and PE represent star-forming and passive galaxies found within our sample, a detailed explanation of how these galaxies were selected will be given in detail in Section 2.5.

Field	RA/DEC	E(B-V)	Eff Area [deg^2]	Galaxies	Stars	SF gzK_s	PE gzK_s
D1	0.2:26:00/-04:30:00	0.0254	0.689	48223	3530	8777	41
D2	10:00:29/+02:12:21	0.0162	0.913	72042	7241	8877	6
D3	14:17:54/+52:30:31	0.0072	0.455	32713	2564	5849	53
D4	22:15:31/-17:44:05	0.0275	0.462	30632	5354	5468	16

Table 2.6: Summary of the four Deep Fields. Effective Areas are given in deg^2 after taking into account external flags. Also shown is a summary of the objects found.

2.4 Selection Criteria

Filters at CFHT, g^* , z' and K_s , differ from those used in the original Daddi selection criteria, (B , z and K_s), Figure 2.4 shows the transmission curves for the Daddi et al. (2004) and the CFHT filters. Due to these differences it is necessary to make a modification to the criteria and develop a gzK_s selection that is alike to the original BzK_s selection criteria. However, since the CFHT observations in g band are too shallow to reliably discriminate between star-forming and passive high-redshift galaxies in the way that the standard BzK_s technique does, we developed a complementary technique based on the $zJHK_s$ filter set. This selection technique will be explained in Section 2.5.

In order to develop a gzK_s selection criteria like the BzK_s selection developed by Daddi et al. (2004) we used SEDfit (Sawicki 2011), a package that enables spectral energy distribution (SED) fitting of photometric data. We specifically used the software program `make_sed` within SEDfit to generate model magnitudes. To generate model magnitudes, SEDfit, starts with rest-frame model spectra from the Bruzual & Charlot library GALEXEV (Bruzual and Charlot 2003). It then performs attenuation by interstellar dust, redshifting to the observed frame and attenuation by intergalactic clouds. Finally the spectra can be integrated using filter transmission curves to produce model magnitudes.

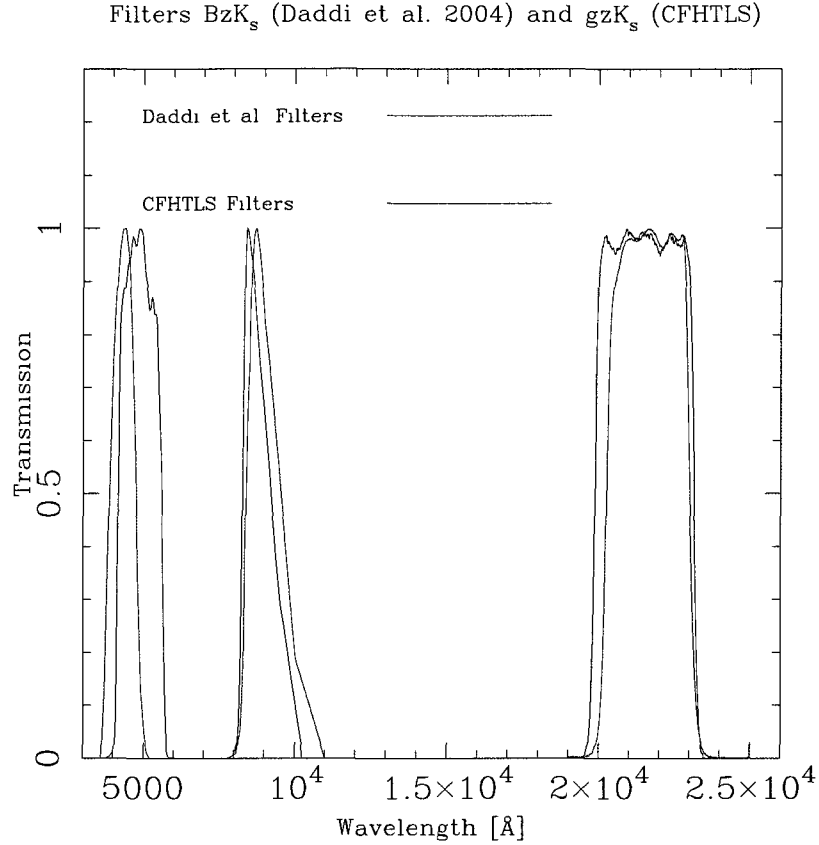


Figure 2.4: Transmission curves for the original BzK_s Daddi filters and the gzK_s CFHTLS-WIRDS filters. From left to right: blue lines: filters B , z and K_s and red lines: filters g , z and K_s

2.4.1 Galaxy Models in the BzK_s and gzK_s Diagrams

As was discussed in Chapter 1, Daddi et al. (2004) developed galaxy evolutionary models in the BzK_s diagram using Bruzual and Charlot (2003) stellar population synthesis models. These models include constant star formation (CSF) and single stellar population (SSP) models to reproduce the colors for star-forming and passive galaxies at $1.4 < z < 2.5$.

A reproduction of these models using SEDfit is shown in Figures 2.5 and 2.6. Models for

star-forming galaxies shown in these figures reproduce ages between 10^{-3} and 2 Gyrs with $0 < E(B - V) < 0.6$. Following Daddi et al. (2004) these models were chosen by considering that star-forming galaxies at $z \sim 2$ will be mainly sampled by galaxies with a young stellar population and some dust.

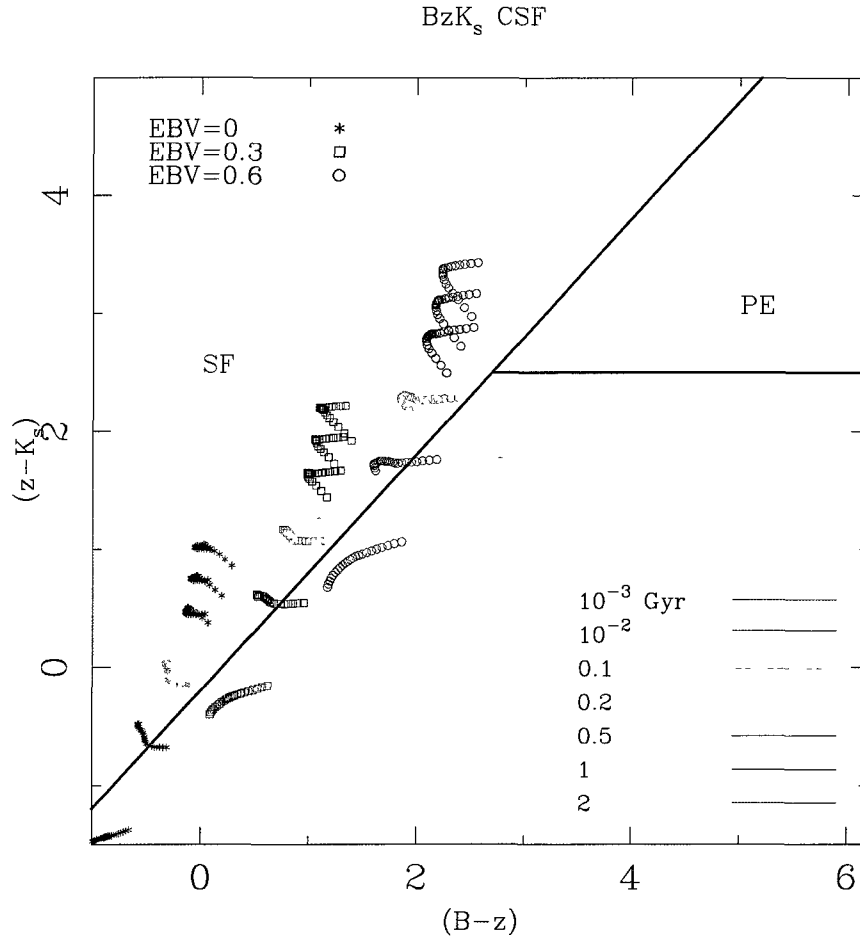


Figure 2.5: *Bruzual and Charlot (2003) stellar population synthesis models for Constant Star Formation (CSF). These models are intended to reproduce BzK_s colors of star-forming galaxies. Ages in Gyr are shown with different colors while $E(B-V)$ are shown with different symbols.*

On the other hand, as seen in Figure 2.6, passive galaxies are reproduced using instantaneous burst models with older stellar populations (ages between 0.1 and 2 Gyrs), and no dust. As explained before in Section 1.2.1, every galaxy that lies to the left of the diagonal line is considered a star-

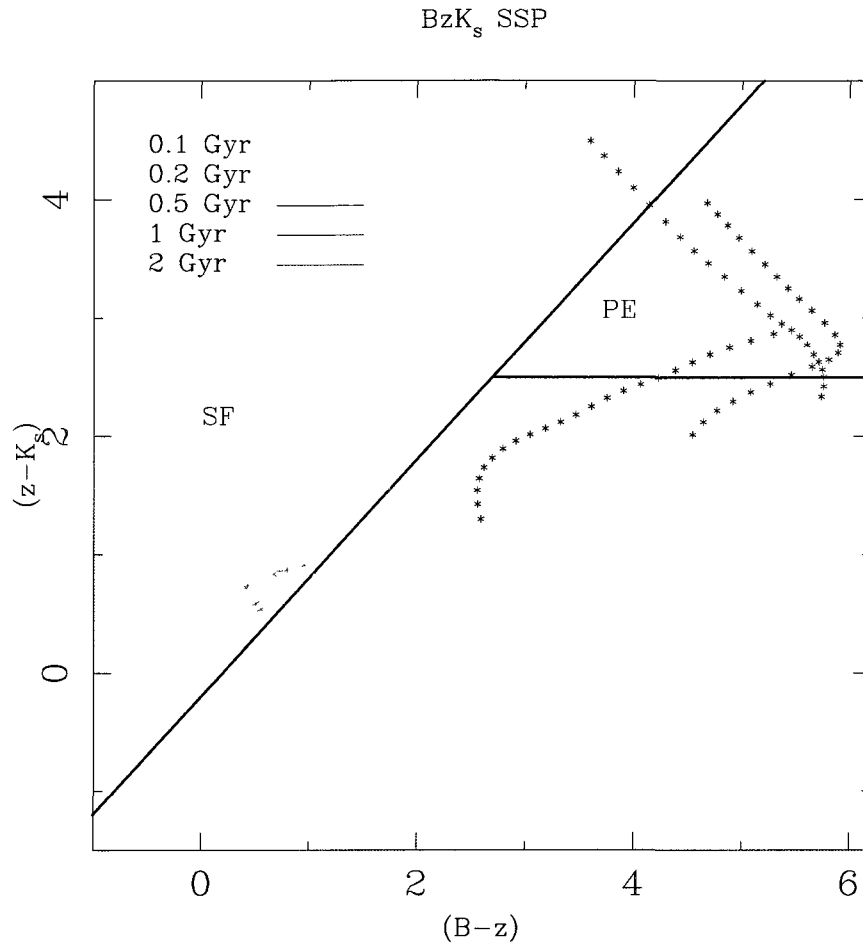


Figure 2.6: *Bruzual and Charlot (2003) stellar population synthesis models for Instantaneous Burst (SSP) Models. These models are intended to reproduce BzK_s colors of passive galaxies. $E(B-V)=0$ for all of the models and different ages are represented with different colors.*

forming galaxy, while everything to the right and above the horizontal line is considered a passive galaxy.

To understand how these models for star-forming and passive galaxies will reproduce under our CFHT set of filters (g , z , K_s), we reproduced these models in a gzK_s color-color selection plot. Figure 2.7 represents the CFHT gzK_s colors of the Daddi et al. (2004) star-forming models of Figure 2.5, while Figure 2.8 represents the gzK_s colors of the passive models of Figure 2.6. Solid

black lines in the gzK_s plots were modified from the original BzK_s lines to select the same models in the gzK_s filter set (See Section 2.4.2).

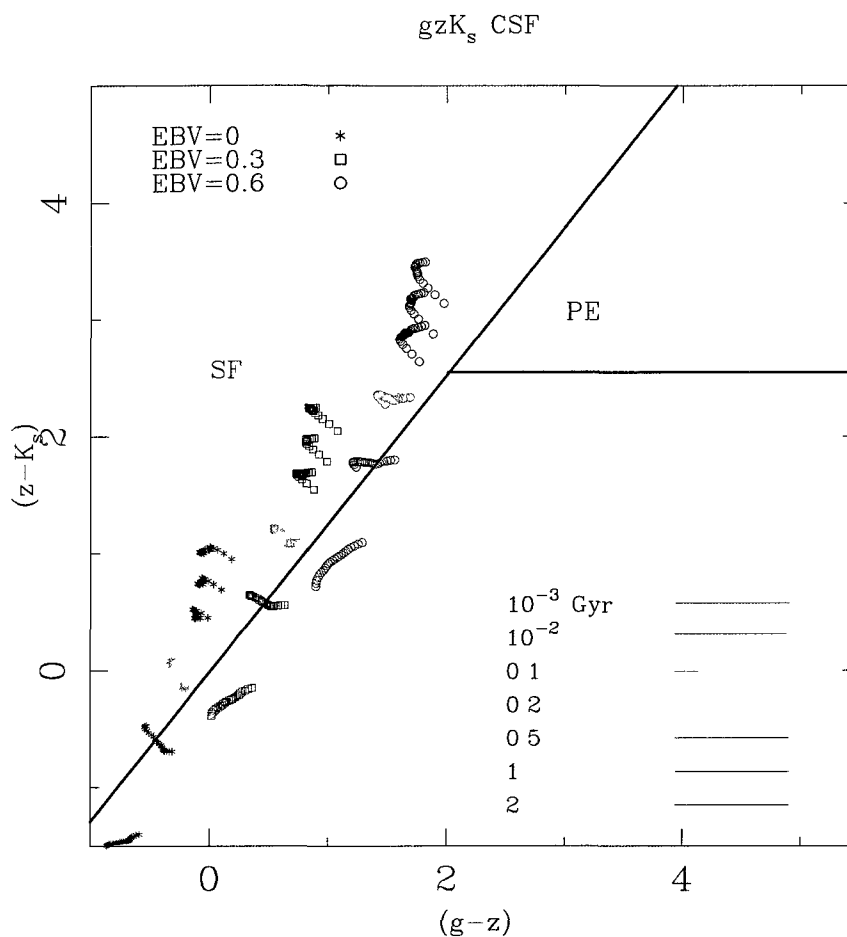


Figure 2.7: *Constant Star Formation Models in the gzK_s color-color plot. Note that the solid black lines that distinguish between star-forming and passive galaxies are not the same as those presented in the Daddi et al. (2004) original selection criteria but they have been adapted to the gzK_s filter set of CFHT.*

As is expected, these gzK_s models reproduce the general trends observed in the BzK_s color-color selection. Star-Forming Galaxies lie to the left of the diagonal line even for those models with $E(B-V)=0.6$. On the other hand, passive galaxies lie to the right of this diagonal line and above the horizontal line. Based on these observations, we can conclude that even though the selection of filters is slightly different, we can adjust the original Daddi et al. (2004) selection and to develop a

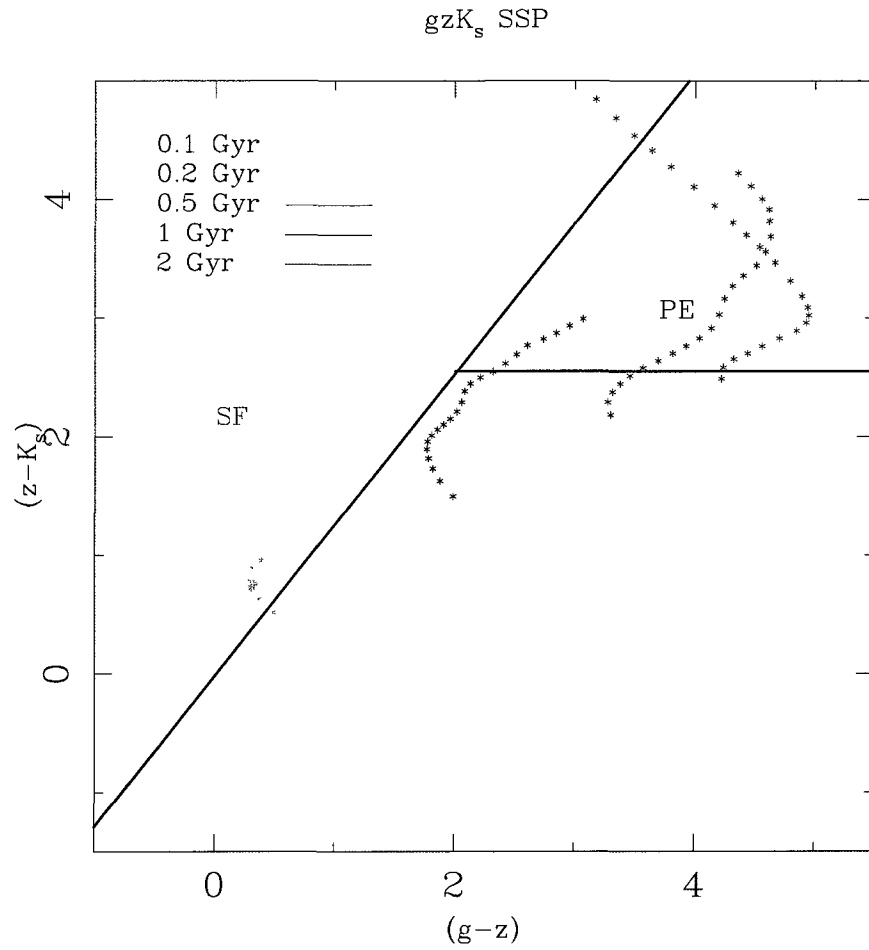


Figure 2.8: *Instantaneous Burst (SSP) Models in the gzK_s color-color plot. As before the solid black lines that distinguish between star-forming and passive galaxies are not the original Daddi et al. (2004) selection criteria but they have been adapted to the CFHT gzK_s filter set.*

gzK_s color-color selection.

2.4.2 Developing the gzK_s Selection Criteria

Using SEDfit, we reproduced galaxy models in the BzK_s diagram and compare these models in the gzK_s diagram to create an adaptation of the original BzK_s selection technique to the CFHT gzK_s filters. Figures 2.9 and 2.10 show the result of our new fitting.

The models in the gzK_s figures with a blue color represent galaxies that, according to their BzK_s colors would be classified as star-forming galaxies. Those with a red color, are passive galaxies in the Daddi et al.(2004) BzK_s diagram, and those marked with yellow color are low redshift galaxies in the BzK_s diagram. Once these models are represented in a gzK_s plot, we can still distinguish a separation between the different populations and develop a new fit that is the closest representation to the Daddi et al. (2004) fit. .

Our new fitting for the gzK_s selection criteria shows that Equation 2.1 will allow us to select star-forming galaxies:

$$(z - K_s) - 1.27(g - z) \geq -0.022. \quad (2.1)$$

To select passive galaxies we use Equation 2.2 while to distinguish between stars and galaxies we use Equation 2.3:

$$(z - K_s) - 1.27(g - z) < -0.022 \quad \cap \quad (z - K_s) > 2.55. \quad (2.2)$$

$$(z - K_s) - 0.45(g - z) \leq -0.57. \quad (2.3)$$

The gzK_s selection criteria that we developed, allows us to select high redshift galaxies in a

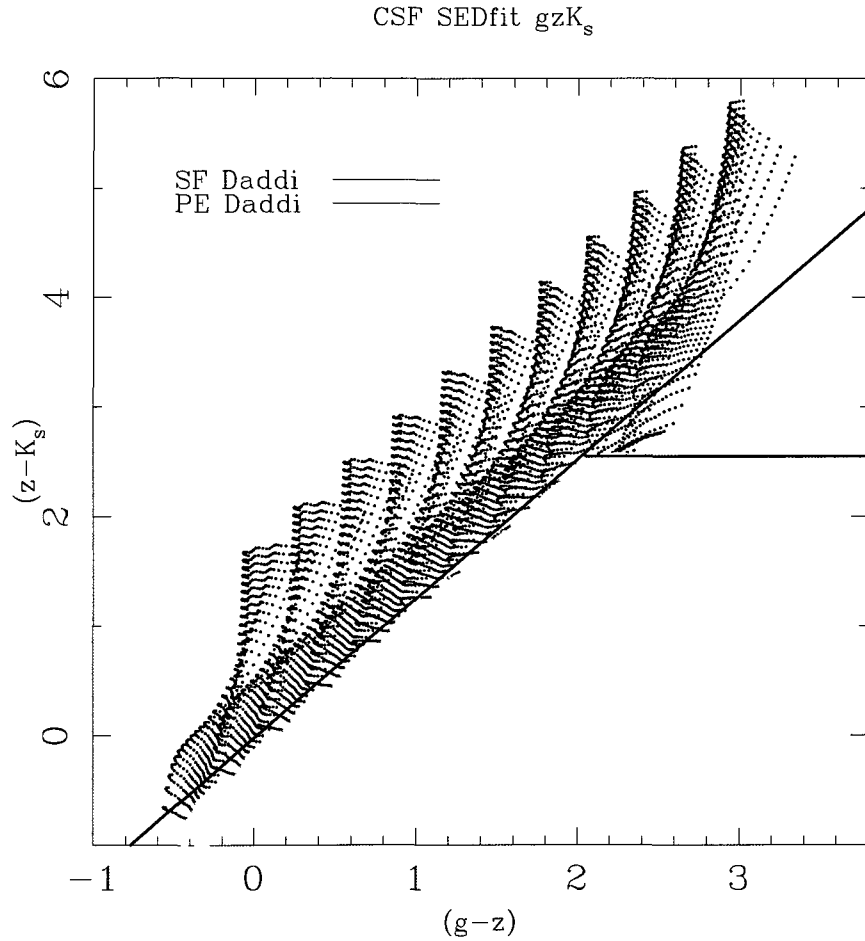


Figure 2.9: gzK_s comparison with BzK_s Constant Star-Formation Models. Blue points, represent galaxies that according to their BzK_s colors are classified as star-forming galaxies. Red points represent passive galaxies in the Daddi et al. (2004) diagram. Finally the yellow points represent low-redshift galaxies. Note that the colors of the galaxies (either blue, red or yellow) which represent if they are either star-forming, passive or low redshift were determined according to their BzK_s classification and these models were plotted in the gzK_s diagram to elucidate the development of a new gzK_s selection criteria.

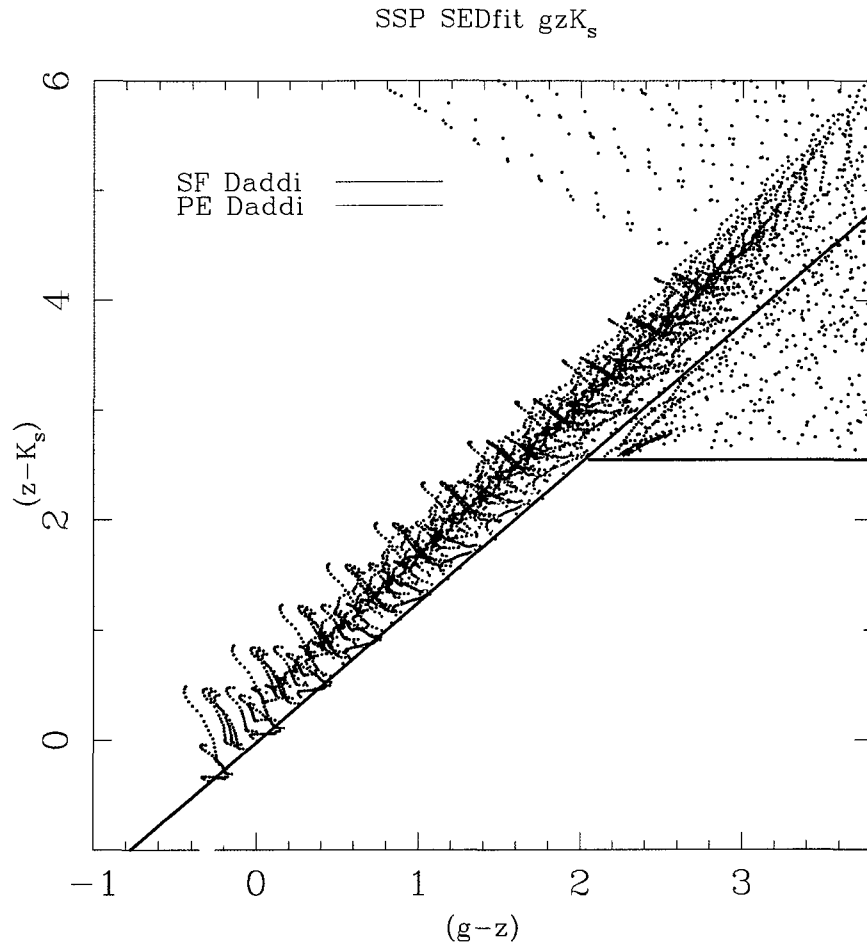


Figure 2.10: gzK_s comparison with BzK_s instantaneous burst models. As in Figure 2.9, blue points represent star-forming galaxies as classified from their BzK_s colors, red points represent passive galaxies as determined by the BzK_s diagram and finally, yellow points are low redshift galaxies in the BzK_s selection criteria.

way that very closely resembles the popular BzK_s technique of Daddi et al. (2004) but is directly applicable to our different CFHTLS filter set.

2.5 ZJHK Selection Criteria

Our gzK_s selection technique allows us to select high redshift galaxies in a manner very similar to that of Daddi et al. (2004). However, since our g-band data is not sufficiently deep, once these objects have been classified as high-redshift galaxies, it is difficult to reliably discriminate between passive and star-forming ones. To solve this deficiency, we developed a second technique based on the zJHK filter set.

Figure 2.11 illustrates the need for an additional criterion: This figure shows a plot of every object in a gzK_s diagram in the region around the division between star-forming and passive galaxies. As the legend in Figure 2.11 shows, objects that have been classified as star-forming according to their gzK_s colors and were detected in g are represented with blue triangles, while those classified as passive galaxies and detected in g are represented as red triangles. Finally, galaxies not detected in g are represented with black arrows. An object is not detected in g if its flux in a circular ten pix aperture is less than the 1σ noise level.

Passive galaxies that were not detected in g are unambiguously passive, while star forming galaxies above the $(z - K_s = 2.55)$ line that were not detected in g could be in fact passive galaxies.

To address this ambiguity above $(z - K_s) > 2.55$, we developed a second selection technique based on the $(z-J)$ versus $(H-K_s)$ colors of galaxies above $(z - K_s) > 2.55$. Taking into account that the main characteristic involved in identifying passively evolving galaxies is their 4000\AA /Balmer break, we try to identify this feature using this color-color selection. However, since we still use the gzK_s selection criteria to select star-forming galaxies below $(z - K_s) < 2.55$ we will have some contamination of low redshift galaxies.

Figure 2.12 shows SEDfit models of star-forming and passive galaxies between redshifts $1.4 \leq$

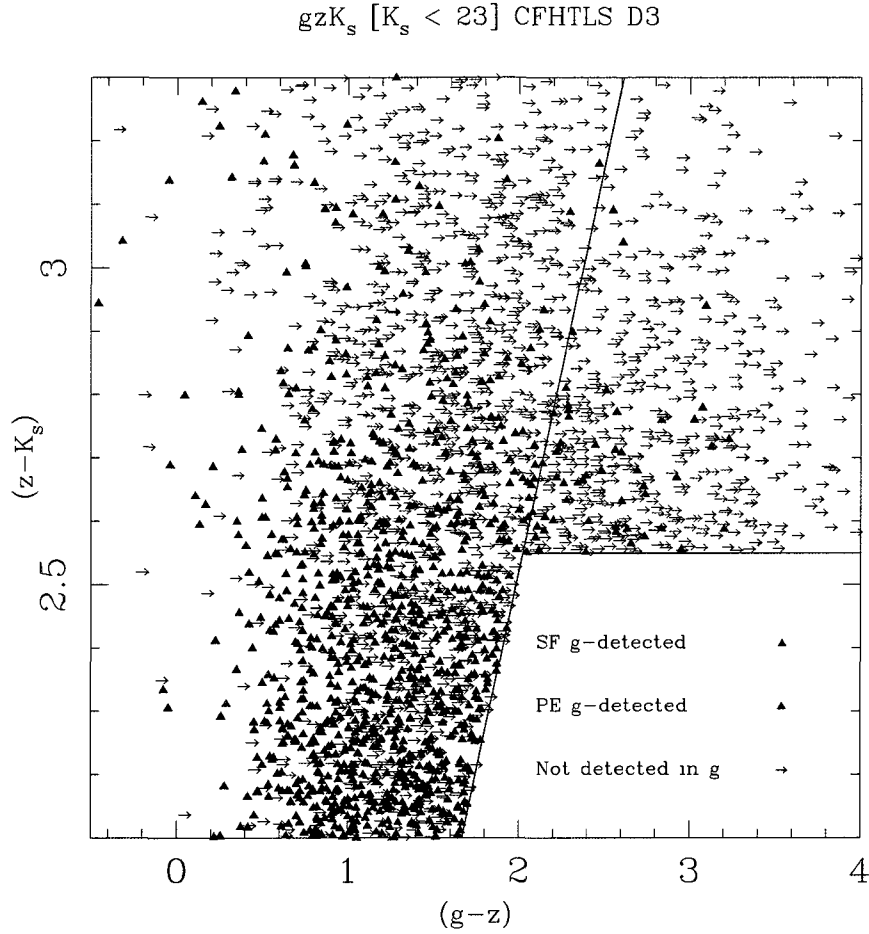


Figure 2.11: g -band non-detections in SF Galaxies in field D3. Galaxies detected in g and classified as star-forming are represented by blue triangles, while galaxies detected in g and classified as passive galaxies are represented by red triangles. Arrows represent 1σ limits for objects that have not been detected in g .

$z \leq 2.5$ above the $(z - K_s) = 2.55$ line. As before (refer to Figures 2.7 and 2.8), for star-forming models we used ages between 0.02 and 2 Gyrs, and $E(B-V) \leq 0$ while for passive galaxies we used models with ages between 0.4 and 2 Gyrs and $E(B-V) = 0$. As can be observed, for a star-forming galaxy, the difference in colors $(z-J)$ and $(H-K_s)$ remains almost a linear relation, this linear relation is attributed to the fact that dust will affect both colors by the same amount and that the spectrum is not expected to have a break. It is also interesting to observe that according to the constant star

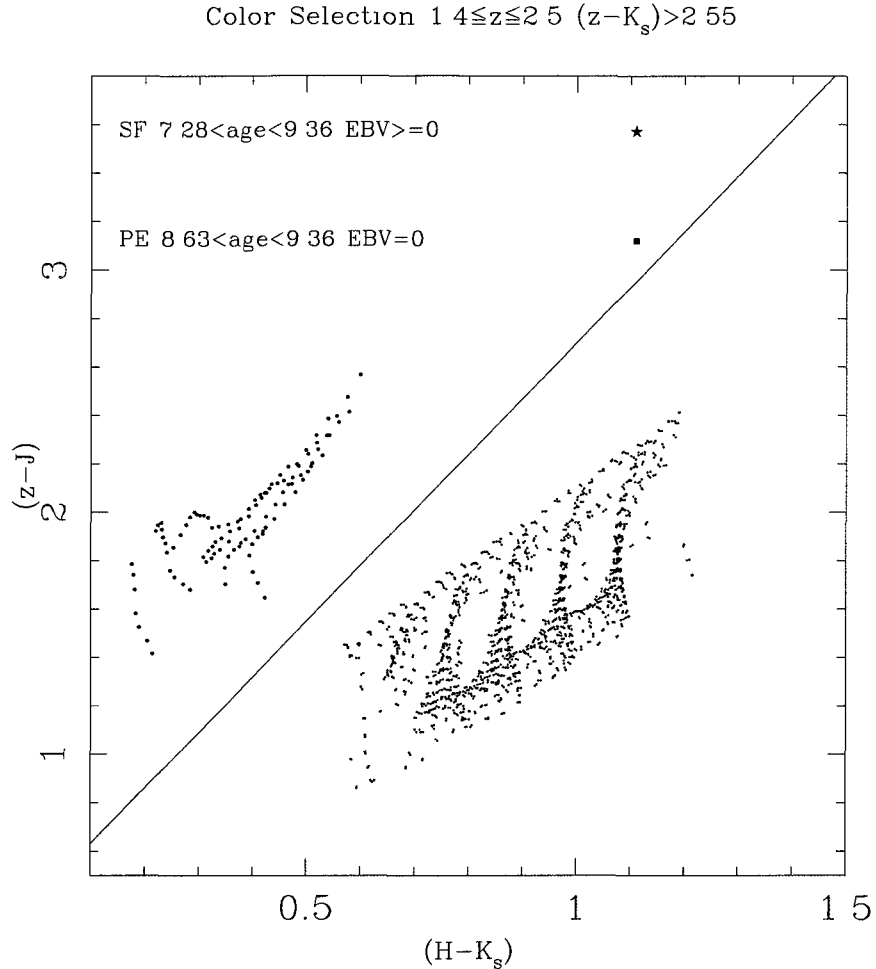


Figure 2.12: *SEDfit* color models for $(z-J)$ versus $(H-K_s)$. Blue models represent star-forming galaxies with $\log_{10}(\text{Age})$ between 7.28 and 9.36 (0.02 and 2 Gyr) and $E(B-V) \geq 0$. Models in red represent passively evolving galaxies with $\log_{10}(\text{Age})$ between 8.63 and 9.36 (0.4 and 2 Gyr) and $E(B-V) = 0$.

formation models, as age or $E(B-V)$ are increased, they evolve parallel to the diagonal line in the $(z-J)$ versus $(H-K_s)$ plot.

On the other hand, if we identify a significant change between colors $(z-J)$ and $(H-K_s)$ this could represent the presence of a break in their spectra. Just as is expected, models that represent passively evolving galaxies lie on a different locus in the plot, where they can be clearly separated from the constant star formation models. At $z \sim 2$ the 4000\AA /Balmer break has been redshifted to 12000\AA and will lie between the z and J filters.

The solid black line in Figure 2.12 represents the division between models of star-forming and passive galaxies above the $(z - K_s = 2.55)$ line. To select star forming galaxies we continue to use the gzK_s colors for galaxies below the $(z - K_s) = 2.55$ line. While galaxies above this line are classified according to their $zJHK_s$ colors using Equation 2.4.

$$(z - J) \leq 2.3(H - K_s) + 0.4. \quad (2.4)$$

To distinguish passive galaxies at $z \sim 2$ that lie above the $z - K_s = 2.55$ line, we used Equation 2.5

$$(z - J) > 2.3(H - K_s) + 0.4. \quad (2.5)$$

Table 2.7 shows a comparison of the different populations in each different field as obtained from $zJHK_s$ and gzK_s selection criteria. In Chapter 3 we will show a comparison of these different criteria (gzK_s and $zJHK_s$) in our results of galaxy number counts and luminosity functions.

Field	SF gzK_s	PE gzK_s	SF $zJHK_s$	PE $zJHK_s$
D1	8777	41	8525	1156
D2	8877	6	10776	1680
D3	5849	53	6336	674
D4	5468	16	5642	841

Table 2.7: Comparison between the different population of galaxies found in each field for the gzK_s and $zJHK_s$ color selection.

Figure 2.13 shows star-forming and passive galaxies in D3 selected using the $zJHK_s$ selection criteria. Symbols are the same as in Figure 2.11, blue triangles are star-forming g-detected gzK_s galaxies, red triangles are passive g-detected gzK_s galaxies while blue triangles represent galaxies not detected in g originally classified as star-forming and red arrows represent galaxies not detected in g that in principle were classified as passive. As seen in Figure 2.13, galaxies that were not detected in g will have a clear classification in the $zJHK_s$ color-color plot: Galaxies to the right of

the solid line are classified as star-forming whereas galaxies that lie to the left of the solid line are classified as passive.

Star-forming and Passive $zJHK$ Galaxies in D3

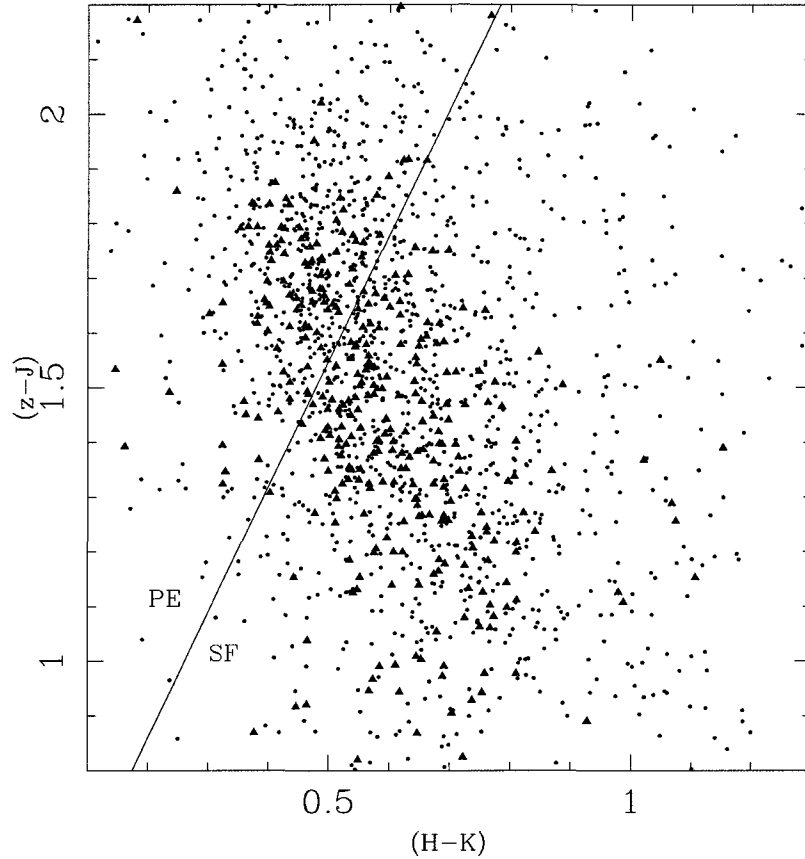


Figure 2.13: $zJHK_s$ star-forming and passive galaxies in D3. Symbols are as in Figure 2.11: Blue triangles represent gzK_s star-forming galaxies that were detected in g , red triangles represent gzK_s passive galaxies that were detected in g and black points represent galaxies that were not detected in g and hence were not initially classified. Using the $zJHK_s$ selection criteria it is possible to classify these non-detections: Galaxies to the right of the solid line are classified as star-forming galaxies, while galaxies to the left of the solid line are classified as passive galaxies.

As a complement to our analysis, we developed a second $zJHK_s$ selection technique which includes models of star-forming galaxies and passive galaxies at $1.4 \leq z \leq 2.5$ with the same characteristics discussed before: ages between 0.02 and 2 Gyr, and $E(B-V) \geq 0$ to represent star

forming galaxies and ages between 0.4 and 2 Gyr, and $E(B-V)=0$ to represent passive galaxies. However, these models not only include $sgzK_s$ galaxies above the $(z - K_s) = 2.55$ line but every possible model that represents a $z \sim 2$ star-forming galaxy. Accordingly, we made an adjustment to the $zJHK_s$ technique which will be called $zJHK_s$ Fit 2.

Figure 2.14 shows our results for Fit 2, and a slightly modified criteria is used to classify the different populations: Equation 2.6 is used to select star forming galaxies while Equation 2.7 is used to select passive galaxies in the $zJHK_s$ color-color diagram. We will present in Chapter 3 number counts for star-forming and passive populations comparing our results obtained with the original $zJHK_s$ fit and our second $zJHK_s$ Fit 2 (see Section 3.1).

$$(z - J) \leq 2(H - K_s) + 0.6. \quad (2.6)$$

$$(z - J) > 2(H - K_s) + 0.6. \quad (2.7)$$

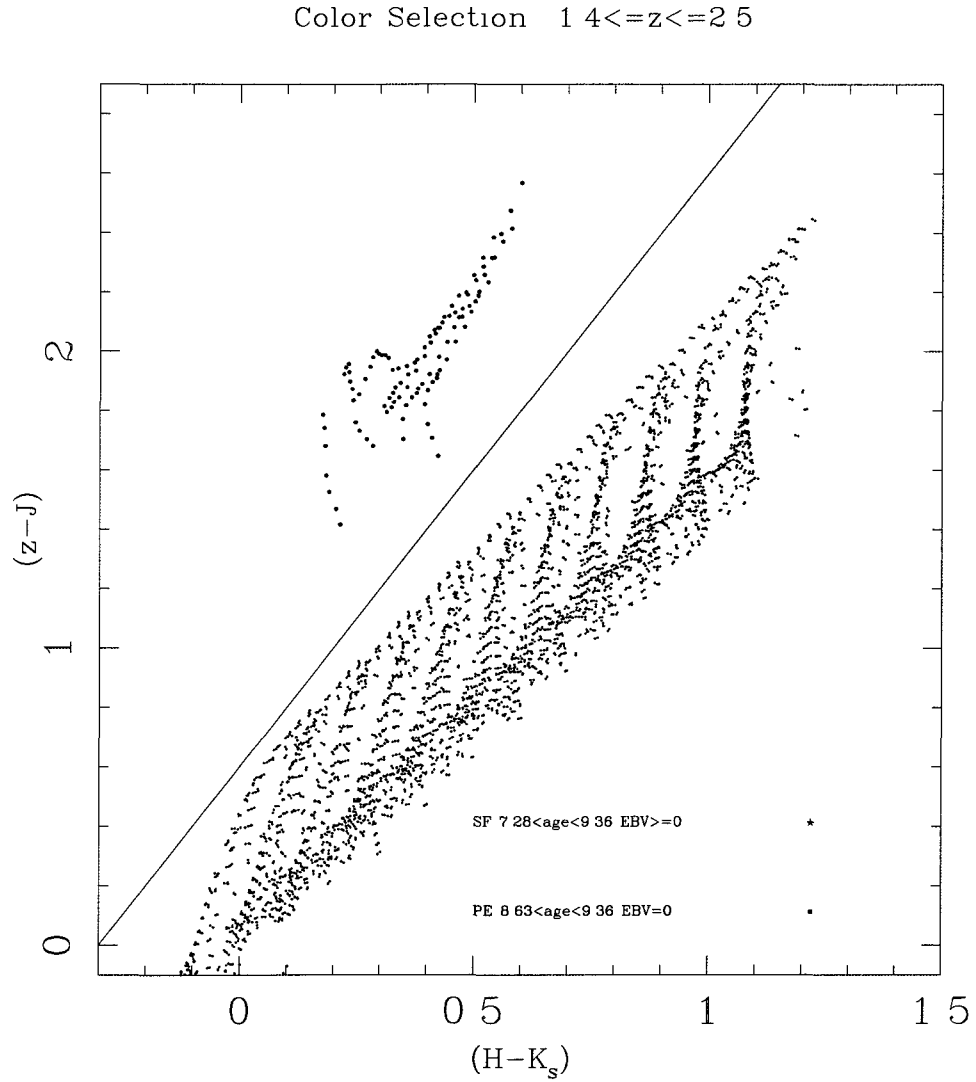


Figure 2.14 $zJHK_s$ color models for star-forming and passive galaxies. As before, to represent star-forming galaxies we used ages between 0.02 and 2 Gyr with $E(B-V) \geq 0$. On the other hand, passive galaxies are represented with ages between 0.4 and 2 Gyr and $E(B-V) = 0$.

Chapter 3

Results

3.1 Galaxy Number Counts

In this chapter we developed galaxy number counts for the different populations of galaxies (all of the galaxies in the field, star-forming and passive galaxies at $z \sim 2$). To do this, we count galaxies in each 0.5 K_s total magnitude bin.

Since faint galaxies are difficult to detect above the fluctuations of the sky, Dr. Taro Sato developed a completeness correction to account for this fact. Using a science image (D1 field), objects were added at random locations in this science image. Then, once SExtractor was used to detect objects in this particular field, it was possible to determine the recovery rate per 0.5 magnitude (to determine how many of the original random extended objects were recovered compared to the original sample). Using these results, the number of galaxies in each 0.5 magnitude bin were re-scaled to correct for this detection efficiency.

Incompleteness corrections are usually of the order of ~ 1.02 between $K_s = 17 - 22$ (AB) magnitudes. As we evolve to fainter magnitudes these corrections become larger. At $K_s=23$ they are larger than two, and this is why our samples were determined up to $K_s < 23$. As a first approximation we used the incompleteness corrections developed for D1 for the rest of the fields. This is a good first approximation since our fields have similar properties but incompleteness

corrections are likely to be underestimated for D2 since this field is not as deep as the rest.

Galaxy number counts for all the galaxies (selected using Equation 2.3) in each field are shown in Figure 3.1. Each symbol represents a different field: Open circles are used to represent galaxies in D1, stars for D2, triangles for D3 and squares for D4. Error bars in this figure shows Gaussian \sqrt{N} uncertainties. To compare our results with other authors, who use the BzK_s selection criteria in K_s -selected galaxies, we included their results in Figure 3.1. A summary for Kong et al. (2006), Lane et al. (2007), Hartley et al. (2008), McCracken et al. (2010) and CFHTLS+WIRDS (survey used in this project), areas and magnitude limits can be found in Table 3.1. As can be seen, our results at faint magnitudes seem to be in good agreement with their results, the small variations between our four fields are most likely due to cosmic variance (i.e. variations in galaxy number density due to small-scale inhomogeneities in the universe).

Nevertheless, at the bright end, ($K_s < 18$) there is significant scatter between surveys. Our results exhibit a bump around $K_s = 15$, this effect could be attributed to a number of reasons: One could be merely due to how SExtractor detects and deals with bright objects. It should also be taken into account that at this bright end, our number counts are relatively low, giving large error bars. Results from Lane et al. (2007) also seem to exhibit a bump at these bright magnitudes, while those of McCracken et al. (2010) do not, and the rest of the authors do not show results at this bright end. Nevertheless, this result is not of great concern since we are mainly interested in the faint end of our galaxy number counts and luminosity functions.

Figures 3.2, 3.3, 3.4 and 3.5 show galaxy number counts of $z \sim 2$ star forming galaxies for fields D1, D2, D3 and D4, respectively, as compared with some different authors (See Table 3.1). Each of these plots show three different results: Blue downward triangles represent galaxies that are secure star-forming gzK_s 's plus those whose star-forming/passive nature is undetermined. This sample represents an upper limit on the number counts for the gzK_s sample, because they include every object in the sample whether or not they were g-detected.

On the other hand, upward blue triangles represent galaxies that are unambiguously star-forming

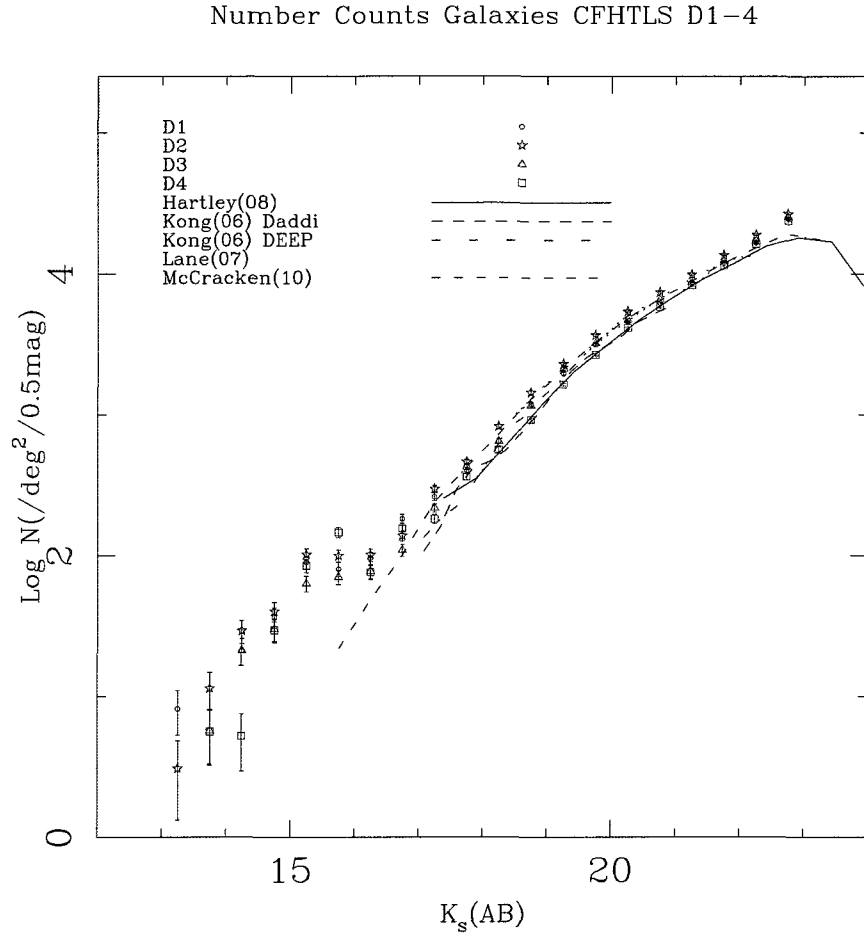


Figure 3.1: *Galaxy Number counts for all the galaxies in each field. Open circles represent D1, stars D2, triangles D3 and squares D4. Our results seem to be in good agreement with other authors and their results of K_s -selected galaxies.*

gzK_s 's. These upward blue triangles represent a lower limit on the number counts of the star-forming gzK_s sample. Finally, the cyan dots represent star-forming galaxies that were selected as star-forming based on their gzK_s colors if they lie below the $(z - K_s) = 2.55$ line and according to their $zJHK_s$ colors if they lie above the $(z - K_s) = 2.55$ line. For simplicity, we refer to these galaxies selected as star-forming galaxies based on their gzK_s and $zJHK_s$ colors according to their position with respect to the $(z - K_s) = 2.55$ as star-forming $zJHK_s$ galaxies.

Figure 3.6 shows galaxy number counts for star-forming $zJHK_s$ galaxies in all fields with

Field	Magnitude limit $K_s(\text{AB})$	Area deg^2
Kong et al. (2006) DEEP Field	22.7	0.08
Kong et al. (2006) Daddi Field	21.5	0.16
Lane et al. (2007)	22.5	0.62
Hartley et al. (2008)	23.5	0.63
McCracken et al. (2010)	23	2
CFHTLS+WIRDS	23	2.51

Table 3.1: K_s Magnitude limits and effective areas for the different authors presented to compare our results. Areas for these different authors are smaller than listed due to masking of bad regions. However, the area presented for this work, CFHTLS+WIRDS is in fact the effective area of the survey after masking of bad regions.

different open blue symbols for each field: circles for D1, stars for D2, triangles for D3, and squares for D4. Also shown as black filled dots are galaxy number counts for star-forming galaxies from averaging all four fields. Both number counts (blue open symbols and filled black symbol) have been slightly shifted horizontally from the bin midpoint for clarity. For the error bars, galaxy number counts for each field (open symbols in blue for each field) were still determined from Gaussian statistics as \sqrt{N} , but error bars for the average fields (filled black circles) are just an estimate of the scatter between the four Deep fields.

Our results seem to be in good agreement with other studies. Our star-forming galaxy number counts in each field seem to be in disagreement with Lane et al. (2007) and Hartley et al. (2008). Lane et al. (2007) attributed the differences between their number counts of star-forming galaxies and other authors such as Kong et al. (2006) to cosmic variance. As seen from our plots, which represent four different fields in the sky, each of which is similar in size to that of Lane et al. (2007), cosmic variance does represent a slight change in galaxy number counts but does not seem to account for such a large difference. Lane et al (2007) and Hartley et al. (2008) used the same data from the UKIRT Infrared Deep Sky Survey (UKIDSS), the only difference being that the newest paper has a deeper version of these data. The difference observed between the galaxy number counts between Hartley et al. (2008) and our results can probably be attributed to an incorrect transformation to the Daddi et al. (2004) system in Hartley et al. (2008) (McCracken et al. 2010).

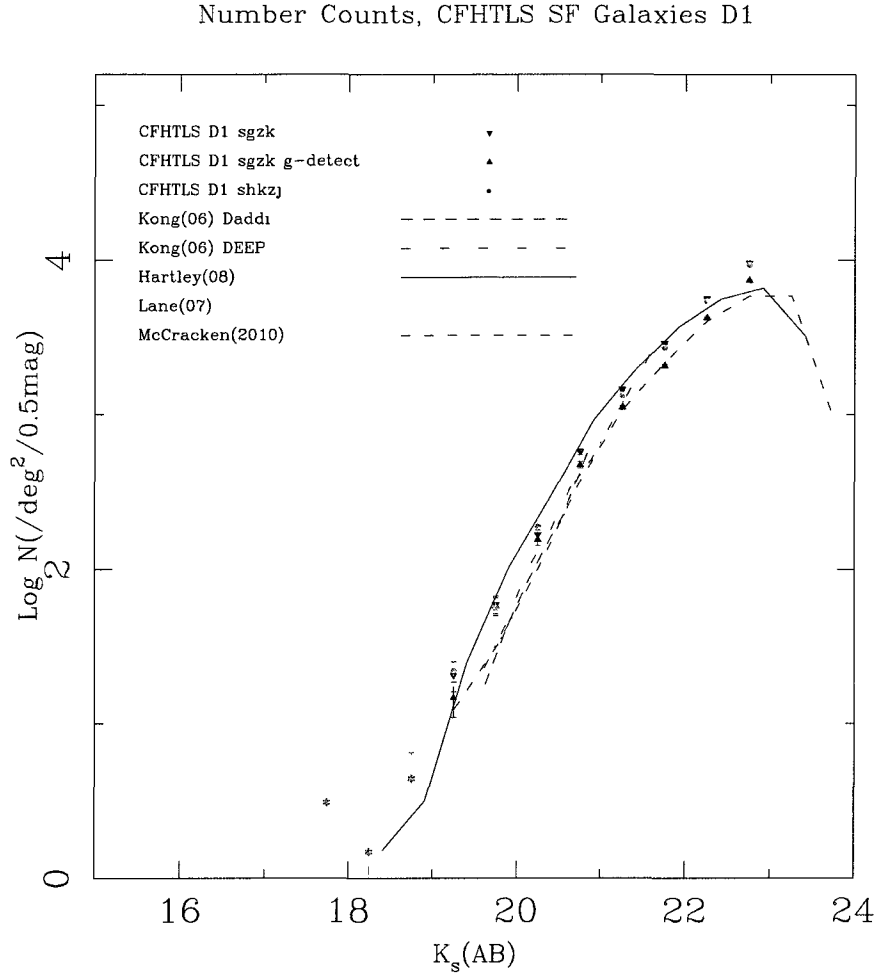


Figure 3.2: Galaxy number counts for star-forming galaxies in field D1. Downward blue triangles are galaxies classified as star-forming based on the gzK_s selection criteria without considering whether or not they were detected in g . Blue upward triangles are also galaxies classified as star-forming based on the gzK_s selection criteria but only those that were g -detected. Cyan circles are galaxies that were selected as star-forming according to their gzK_s color if they lie below the $(z - K_s) = 2.55$ line, while those lying above this line were classified as star-forming according to their $zJHK_s$ colors. Also shown are the results from several different authors that used the BzK_s selection criteria to classify K_s selected galaxies as star-forming.

Galaxy number counts for passive galaxies in each field are shown in Figures 3.7, 3.8, 3.9 and 3.10. As before, each plot shows three different results for the galaxy number counts: Orange downward triangles represent galaxy number counts of secure passive gzK_s galaxies and those gzK_s whose star-forming/passive nature is undetermined. This population represents an upper limit

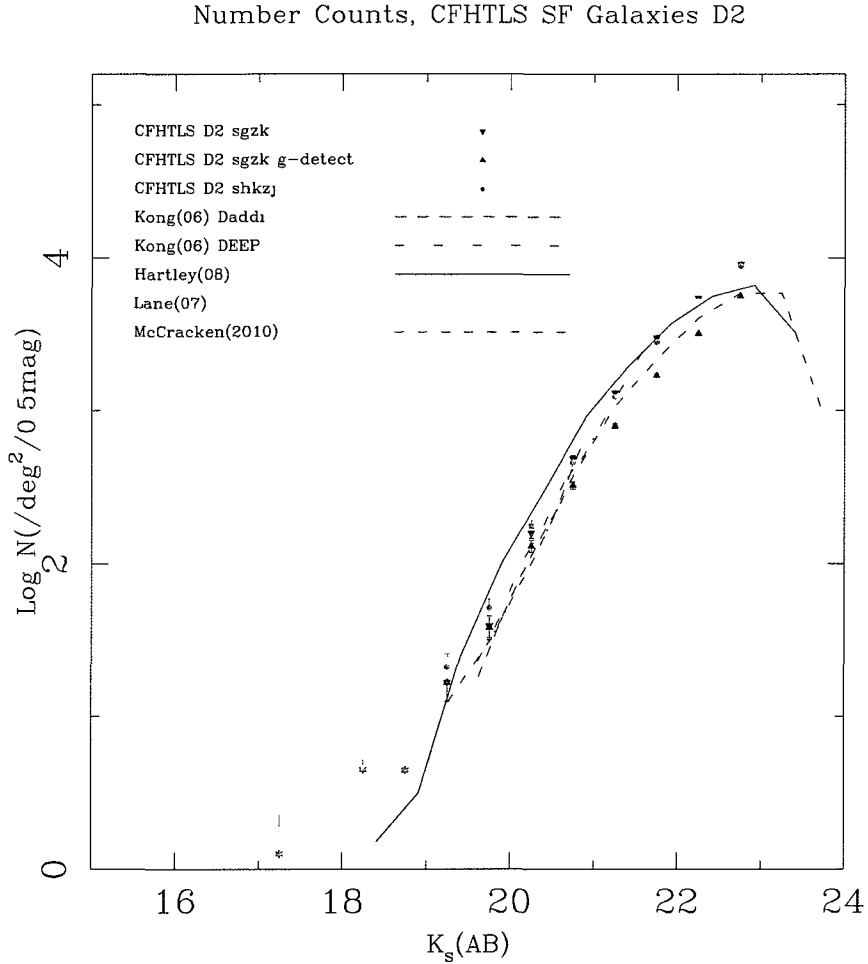


Figure 3.3: *Galaxy number counts for star-forming galaxies in field D2. Symbols are the same as in Fig 3.2.*

for the gzK_s population.

Upward orange triangles represent only secure passive gzK_s 's and so represent a lower limit of the $z \sim 2$ passive galaxy number counts. Finally, red circles represent galaxies above the $(z - K_s) = 2.55$ line that were classified as passive galaxies according to their $zJHK_s$ colors. Error bars for these three different result are determined as before from Gaussian statistics as \sqrt{N} .

As before, we compared our results with those of several different authors that used the BzK_s selection technique. As a special feature for Hartley et al. (2008) and McCracken et al. (2010), we

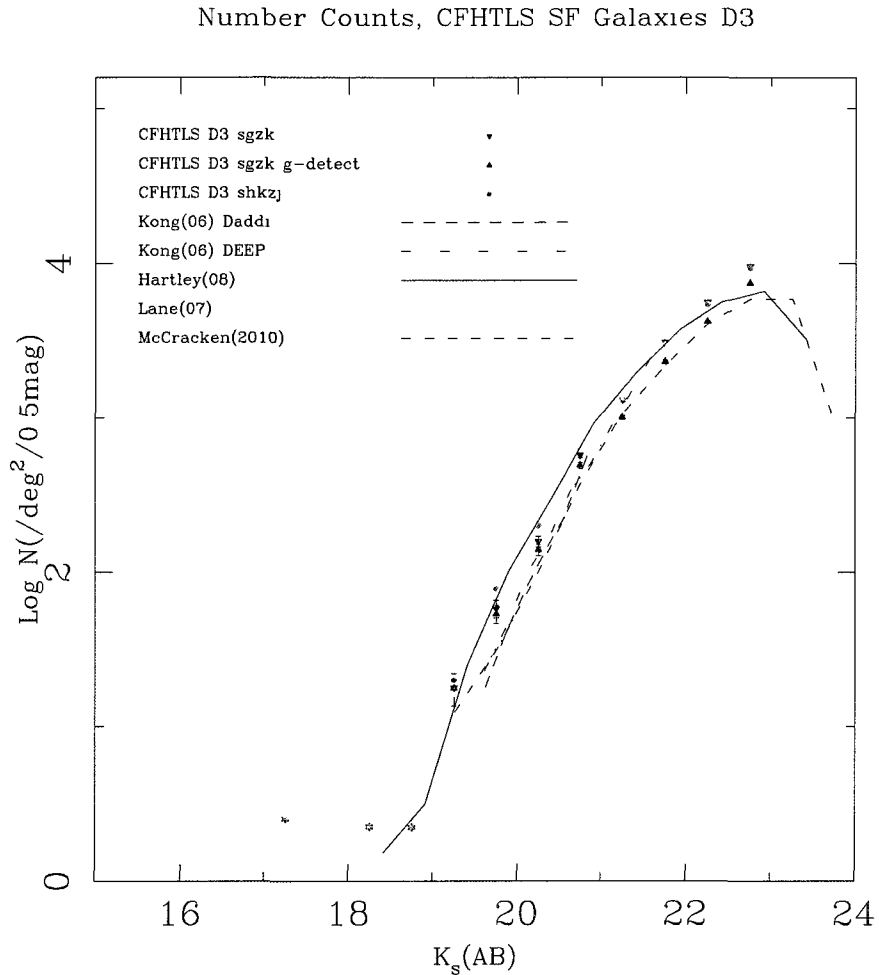


Figure 3.4: Galaxy number counts for star-forming galaxies in field D3. Symbols are the same as in Fig 3.2.

included a second red line that represents their “upper limit”: Specifically for Hartley et al. (2008) this upper limit is a scenario in which all of their non-detections in B and z’ were in fact passive galaxies and they include all of these objects in their red line. As can be seen, compared with their solid black line, their solid red line exhibits a flattening in their number counts at faint magnitudes, but once they account for these “extra” objects, the turnover disappears before their $K_s = 23.5$ limit.

For McCracken et al. (2010), the red dot-dash line represents those galaxies that were classified

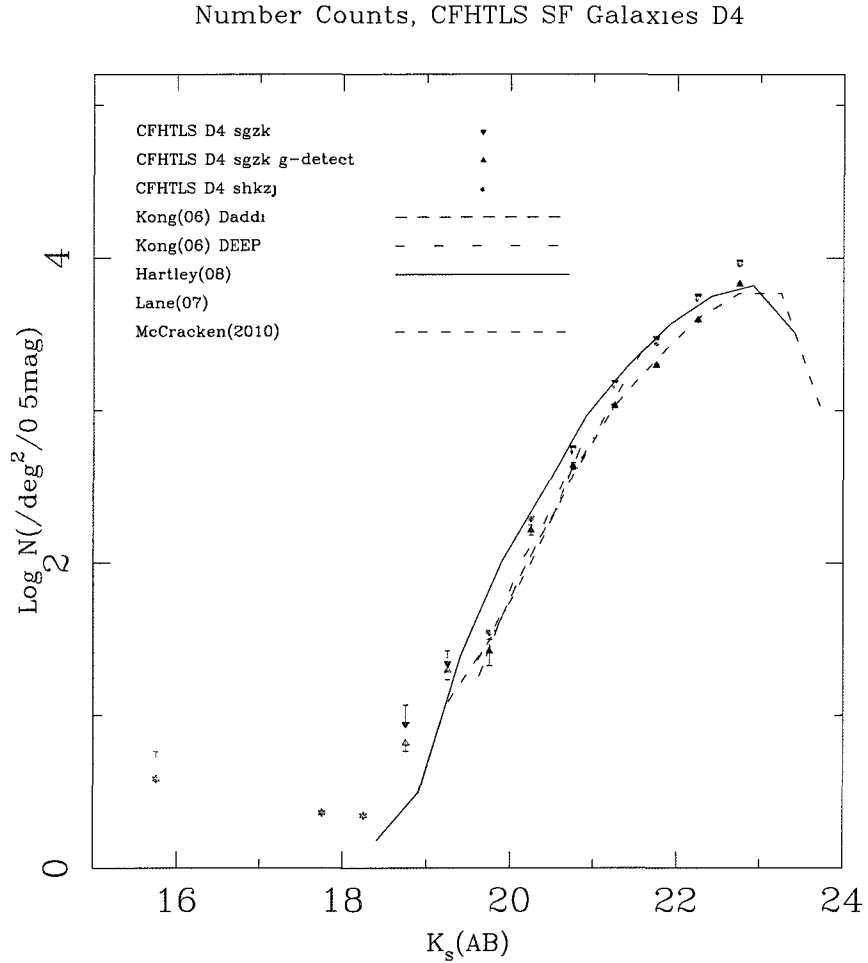


Figure 3.5: *Galaxy number counts for star-forming galaxies in field D4. Symbols are the same as in Fig 3.2.*

as passive based on their BzK_s colors and star-forming galaxies above the $(z - K_s) = 2.5$ line that were not B-detected. As can be observed, even taking into account this worst case scenario, they observe a flattening in the number counts at faint magnitudes AND a turnover, which Hartley et al. (2008) do not see. As was explained before, downward triangles in our galaxy number counts include an “upper limit” in which we include in the passive population, detected $pgzK_s$ galaxies and gzK_s galaxies whose star-forming/passive identities are ambiguous.

Galaxy number counts for $z \sim 2$ JHK_s passive galaxies in all four CFHTLS Deep fields are

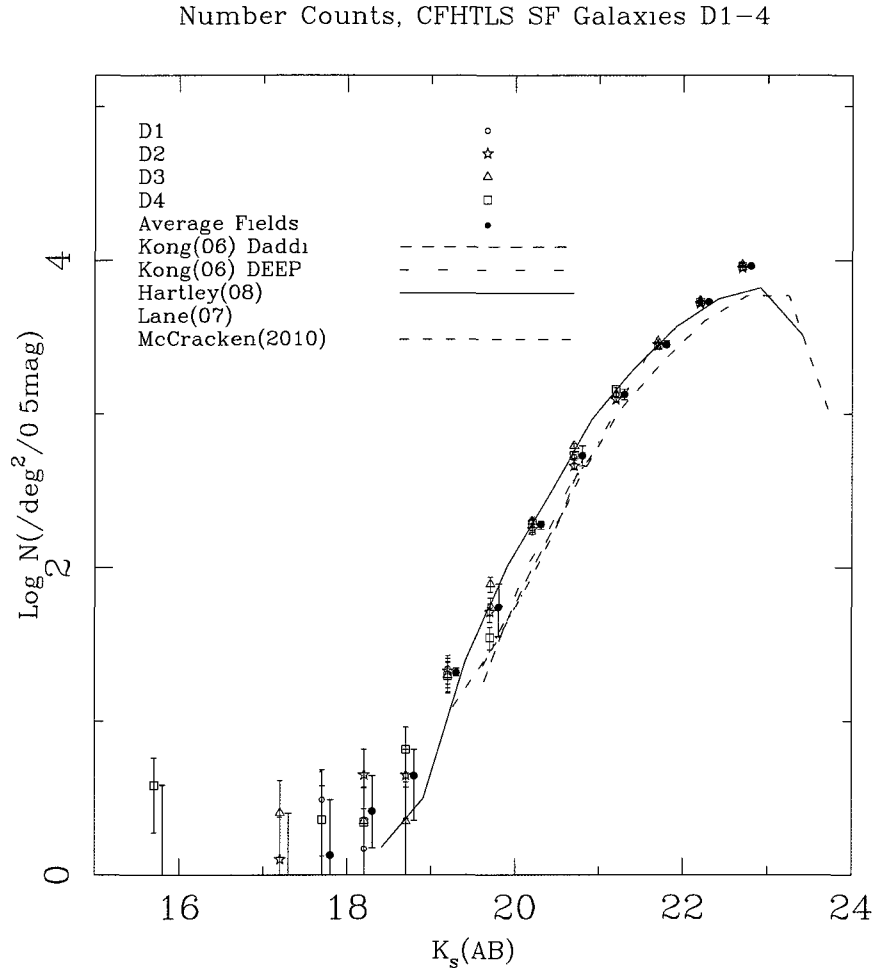


Figure 3.6: Galaxy number counts for star-forming galaxies selected using their gzK_s colors if they lie below the $(z - K_s) = 2.55$ line and their $zJHK_s$ if they lie above this line. Open blue symbols represent our four Deep fields D1-4, error bars were determined from Gaussian Statistics. Also shown in filled black circles are galaxy number counts for the average of our four fields fields. Error bars are an estimate of the scatter between fields for this sample. Both open blue symbols and black filled circles were shifted horizontally from the midpoint of the bin for clarity.

shown in Figure 3.11. Each field is represented with a different open symbol: circles for D1, stars for D2, triangles for D3 and open for D4, as before, error bars are \sqrt{N} . Also shown as black filled circles are galaxy number counts for the average fields with error bars given as an estimate of the scatter in number counts between the four fields.

Our results seem to be in good agreement with other studies, especially with McCracken et

Number Counts PE Galaxies CFHTLS D1

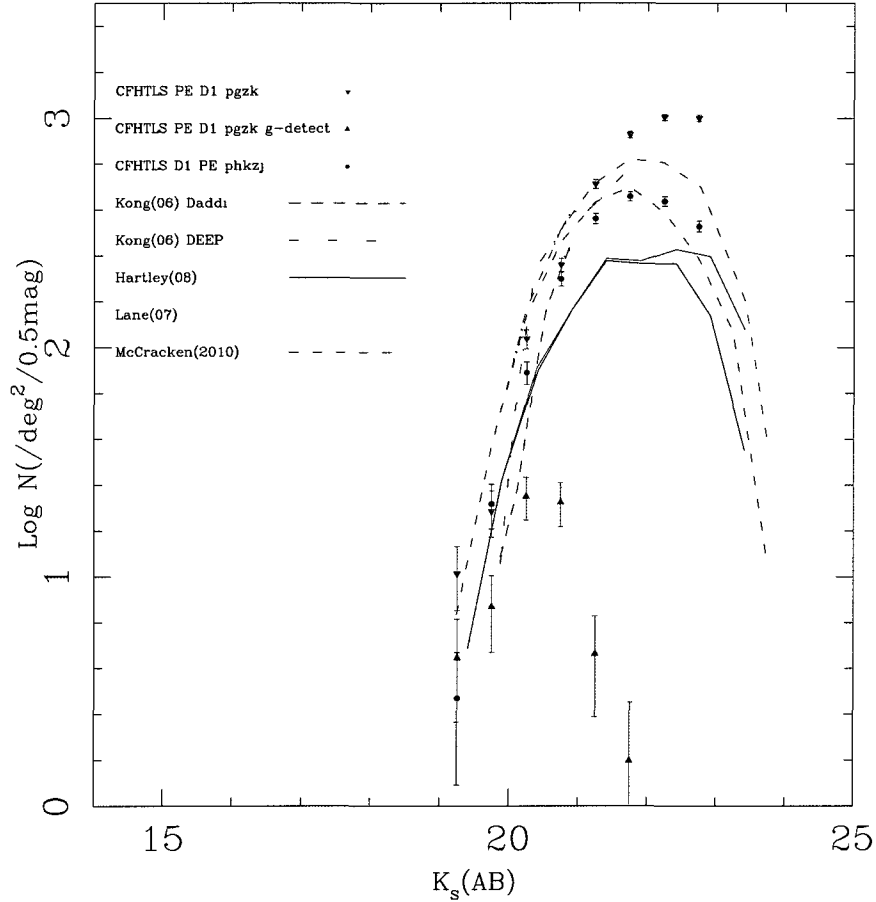


Figure 3.7: Galaxy number counts for passive in field D1. Orange downward triangles represent gzK_s passive galaxies and star-forming gzK_s galaxies above the $(z - K_s) = 2.55$ line that were not detected in g . Upward orange triangles represent galaxies that were classified as passive based on their gzK_s colors but only those that were g -detected. Red circles represent galaxies that were classified as high-redshift based on their gzK_s colors and then were classified as passive based on their $zJHK_s$ colors. Also shown are results from several different authors, including a best and worst case scenarios for Hartley et al. (2008) and McCracken et al. (2010).

al. (2010): Galaxies selected using the $zJHK_s$ criteria lie in between their two limits (black and red lines). Our results do not seem to agree with Hartley et al. (2008). McCracken et al. (2010) attributed this difference of galaxy number counts between Hartley et al. (2008) and other authors due to an incorrect transformation to the Daddi et al. (2004) system in the Hartley et al. (2008) paper. From our results we also observe a flattening in the galaxy number counts of passive galaxies

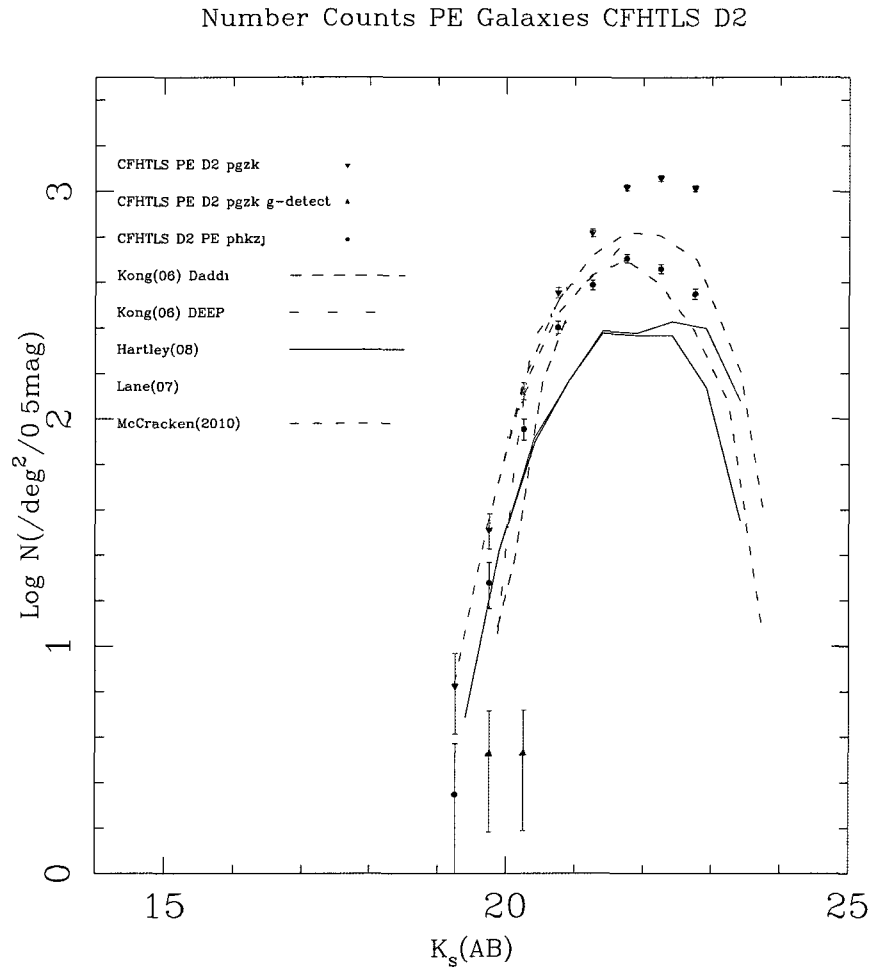


Figure 3.8: *Galaxy number counts for passive galaxies in field D2. Symbols are the same as in Fig 3.7.*

at faint magnitudes and a possible turnover. This turnover is clearly present in some of our fields, but not in others. For example, in D2 this turnover is clear which is consistent with the results found by McCracken et al. (2010) since D2 overlaps with their field (COSMOS Field). Note that our number counts for D2 are somewhat inaccurate because of our use of D1 for our incompleteness corrections.

The presence of the turnover seems dependent on location, as it is present in some fields but not in others. This fact only becomes apparent when analysing multiple fields at the same time like we do in the CFHTLS. Another interesting feature in our number counts is that some fields, such as

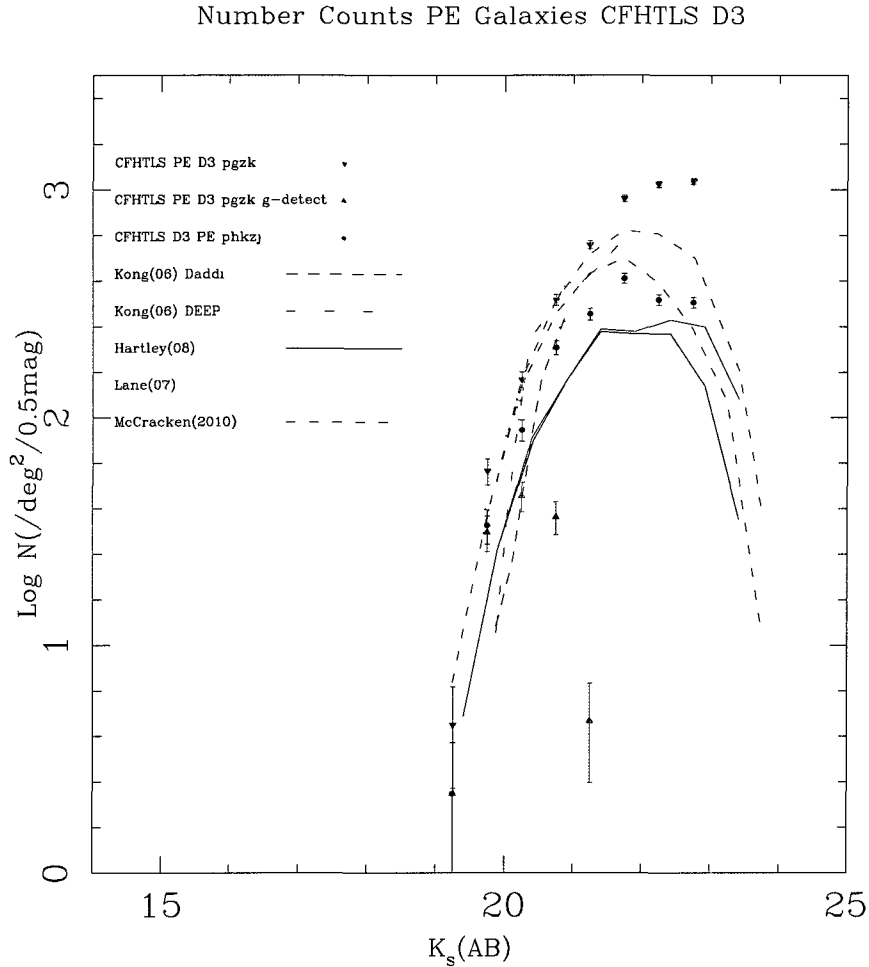


Figure 3.9: *Galaxy number counts for passive galaxies in field D3. Symbols are the same as in Fig 3.7.*

D3, appear to be underdense (refer to Figure 3.11), this could again be a manifestation of cosmic variance.

Finally, we show a comparison in the galaxy number counts for star-forming and passive galaxies between our original $zJHK_s$ fit and our second $zJHK_s$ developed to include models of star-forming galaxies below the $(z - K_s)$ horizontal line. Figure 3.12 shows a comparison of the two different fits for the number counts of average star-forming galaxies in our four Deep fields. Figure 3.13 shows the same comparison between our original $zJHK_s$ fit and Fit 2 (see Section 2.5) for the number

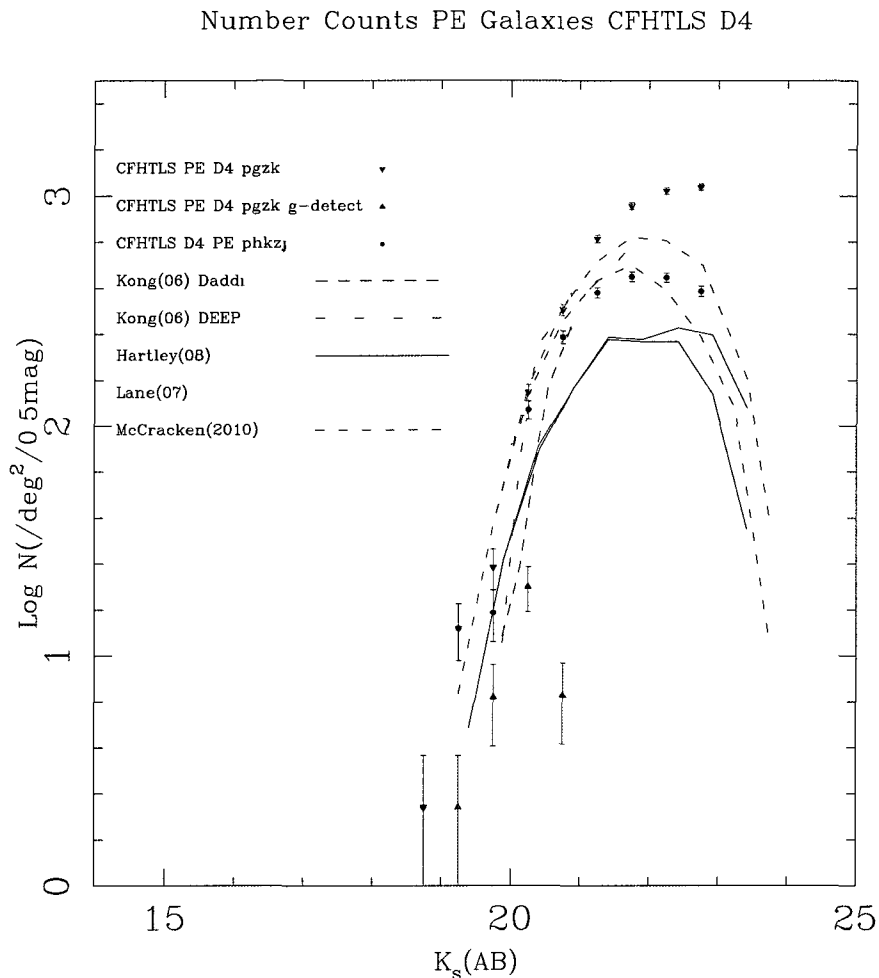


Figure 3.10: *Galaxy number counts for passive galaxies in field D4. Symbols are the same as in Fig 3.7.*

counts of the average passive galaxies in our four Deep Fields. As can be observed in both figures, our galaxy number counts for star-forming galaxies increase slightly while the galaxy number counts for passive galaxies decreases. Nevertheless, our results for Fit 2 still agree with most authors and we still observe a flattening and a possible turnover in our galaxy number counts for passive galaxies.

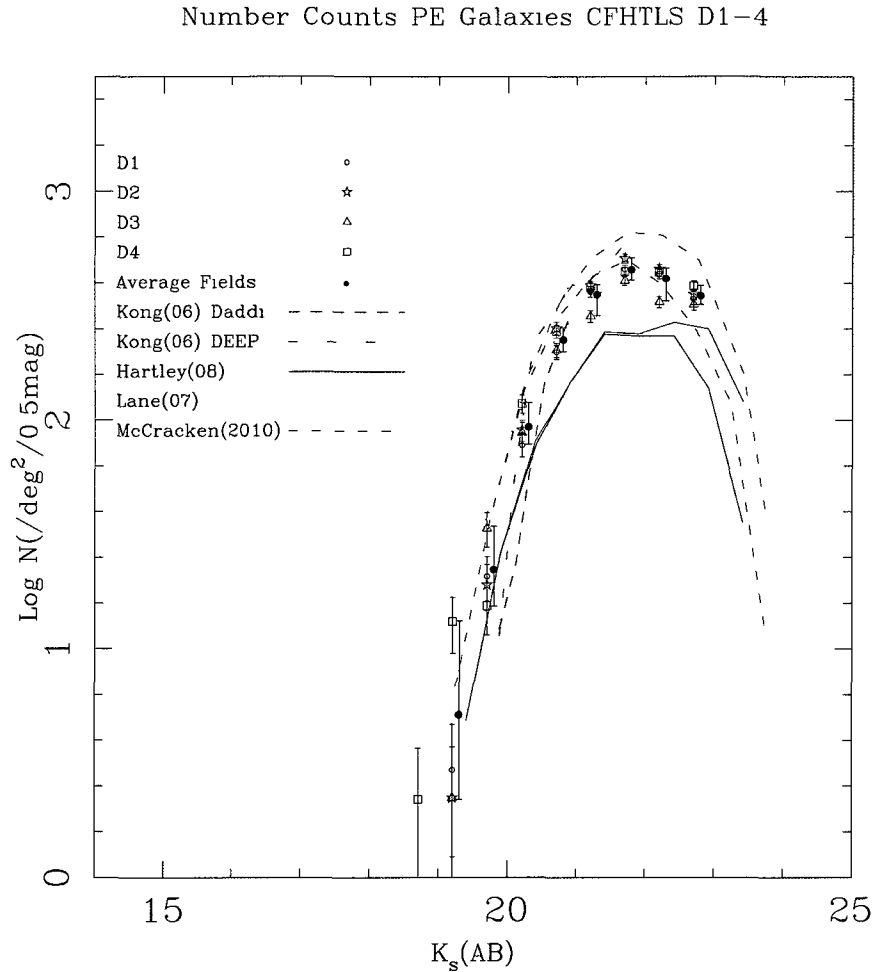


Figure 3.11: *Galaxy number counts for $z \sim 2$ passive galaxies selected using the $zJHK_s$ selection criteria. Open red symbols represent our four Deep fields D1-4. Error bars were determined from Gaussian Statistics. Also shown in filled black circles are galaxy number counts for the average of our four fields, for which error bars are an estimate of the scatter between fields for this sample. Both open red symbols and black filled circles were shifted horizontally from the midpoint of the bin for clarity.*

3.2 Luminosity Function

In this section, we will discuss how we developed rest-frame R luminosity functions for our $z \sim 2$ star-forming and passive galaxies. Note that a rest-frame R luminosity function is alike to a mass function since rest-frame R emission ($\sim 6000\text{\AA}$) will come mainly from low-mass stars, which

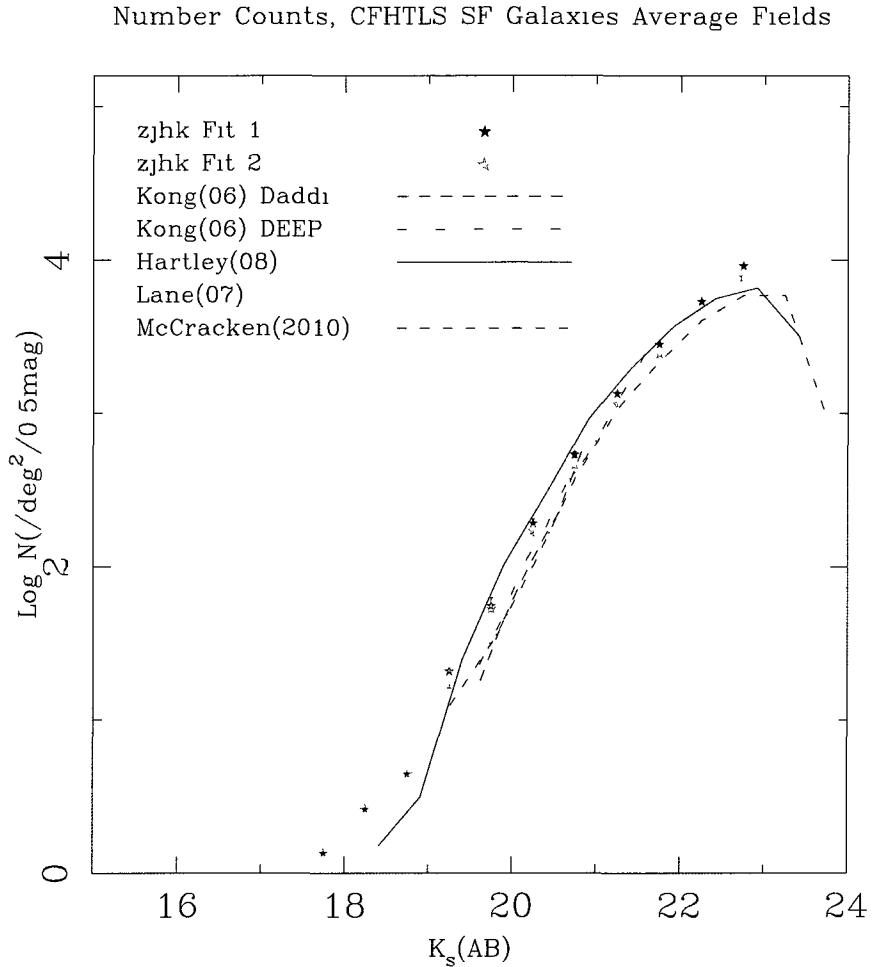


Figure 3.12: *Galaxy number counts for $z \sim 2$ star-forming galaxies for our original $zJHK_s$ fit and complementary $zJHK_s$ Fit 2 (See Chapter 2). Dark blue stars represent number counts for our original $zJHK_s$ fit while cyan stars represent galaxy number counts for our $zJHK_s$ Fit 2. As before, we also present results for several different BzK_s surveys.*

dominate the stellar mass of a galaxy.

There are several steps involved in developing our luminosity function: first we must correct our number counts for detection incompleteness, then we must estimate the volume of our sample by assuming a redshift range, and finally convert our apparent magnitudes to absolute ones.

As was mentioned in the procedure developed for our number counts, incompleteness due to detections was already addressed by implanting extended objects at random positions in our fields

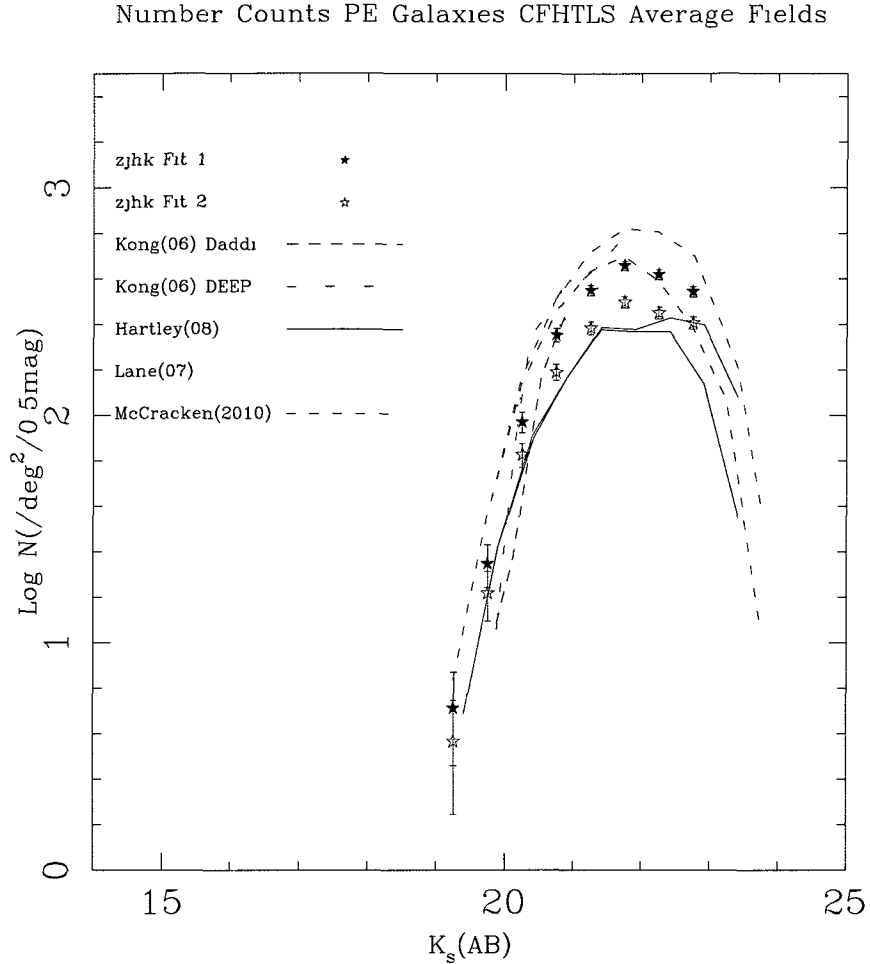


Figure 3.13: Galaxy number counts for $z \sim 2$ passive galaxies for our original $zJHK_s$ fit and complementary $zJHK_s$ Fit 2. Red stars represent passive galaxies selected with our original $zJHK_s$ fit while orange stars represent passive galaxies selected with the complementary $zJHK_s$ Fit 2.

and then attempting to recover them using SExtractor (see Section 3.1).

3.2.1 Effective Volumes

A definition of effective volume, V_{eff} , is given in Equation 3.1

$$V_{\text{eff}}(m) = \int \frac{dV}{dz} p(z) dz, \quad (3.1)$$

where $p(z)$ is the sample completeness function and dV/dz is the comoving volume per square degree. Several corrections must be taken into account when calculating an effective volume, as was explained before, one of these corrections is incompleteness due non-detections (this correction was provided by the recovery rate of extended objects added at random positions in the science images) and scatter of galaxies in and out of the different regions in our gzK_s color-color plot. Our procedure to calculate the effective volume or V_{eff} is different from the original approach developed by Steidel et al. (1999) and Sawicki & Thompson (2006) since we do not include an estimate of photometric scatter in our populations.

To calculate $p(z)$ we developed color models for galaxies using Bruzual & Charlot (1993) spectral synthesis models for star-forming and passive galaxies. Figure 3.14 shows color models in a gzK_s plot for star-forming galaxies. As before, we selected models that would resemble the real characteristics of a star-forming galaxy: ages from 0.1 to 2 Gyr and three different values of $E(B-V)=0.1, 0.3, 0.6$. Models with the same age have the same color, and different $E(B-V)$ were represented with different symbols, as can be seen in the color models, as $E(B-V)$ and age increase, the models evolve parallel to the diagonal line used in our selection criteria. Redshift on the other hand evolves from the right to the left and upward in the diagram as seen in the figure by the black arrow.

From Figure 3.14 we can determine a probability box $p(z)$ (see Figure 3.15) for which (as a first approximation) we will give a probability of 1 to the redshift range in each model that lies left of the diagonal line, and a probability of 0 to every redshift to the right of the diagonal line. As explained before, every galaxy that lies to the left of the diagonal line should represent a star-forming galaxy. Accordingly, considering that each model has a redshift range that goes from 0 to 4, as redshift evolves in each one of these models, we created a value for $p(z)$ according to whether or not this redshift lies to the left or to the right of the diagram.

This probability box, $p(z)$ represents the values that we will use in the integral for the effective

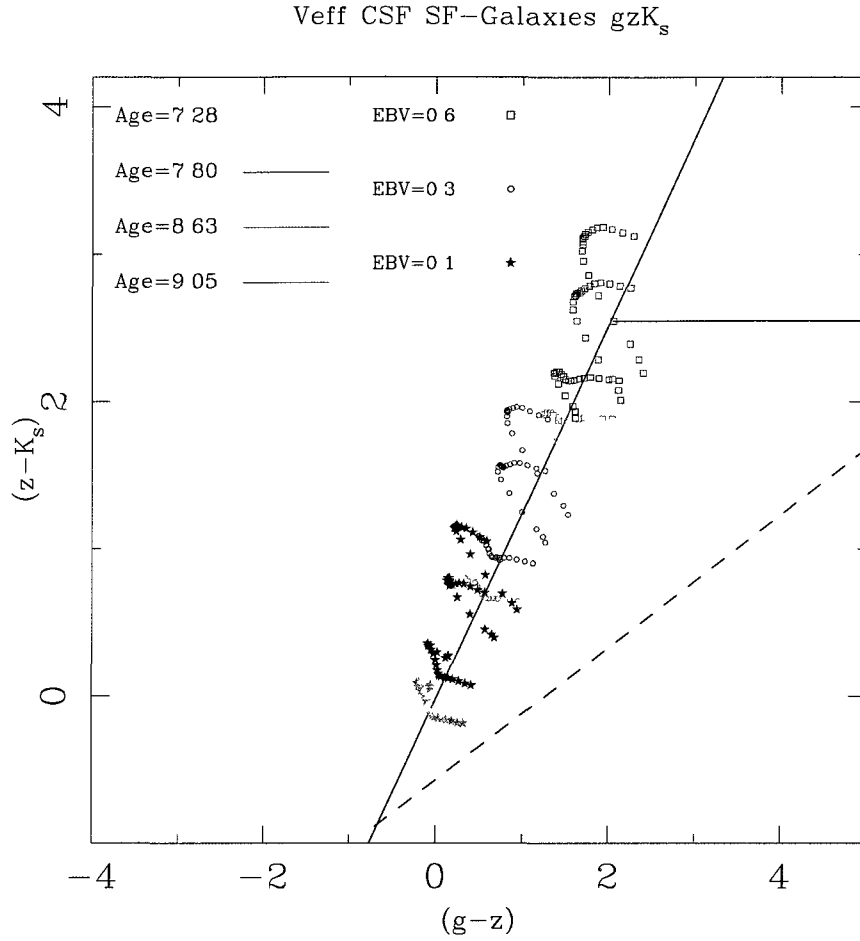


Figure 3.14: Color gzK_s Models from Bruzual & Charlot (1993) spectral synthesis models for star-forming galaxies. Ages range from 0.1 to 2 Gyr and three different models for $E(B-V)=0.1, 0.3, 0.6$. Models with the same age have the same color but different $E(B-V)$ are represented with different symbols. As $E(B-V)$ increases, the model evolves parallel to the diagonal line.

volume, as seen in Equation 3.1. To determine the differential comoving volume, we used `perIDL` (Glazebrook & Economou 1997) built-in function `dcomov_vol` as a function of redshift.

By definition, our $zJHK_s$ selection criteria were developed using galaxy color models in the $(z - J)$ versus $(H - K_s)$ color-color plot for galaxies that are classified as star-forming and passive according to their gzK_s colors. This is why the estimate of effective volume for our gzK_s populations is the same as the one used in our $zJHK_s$ sample.

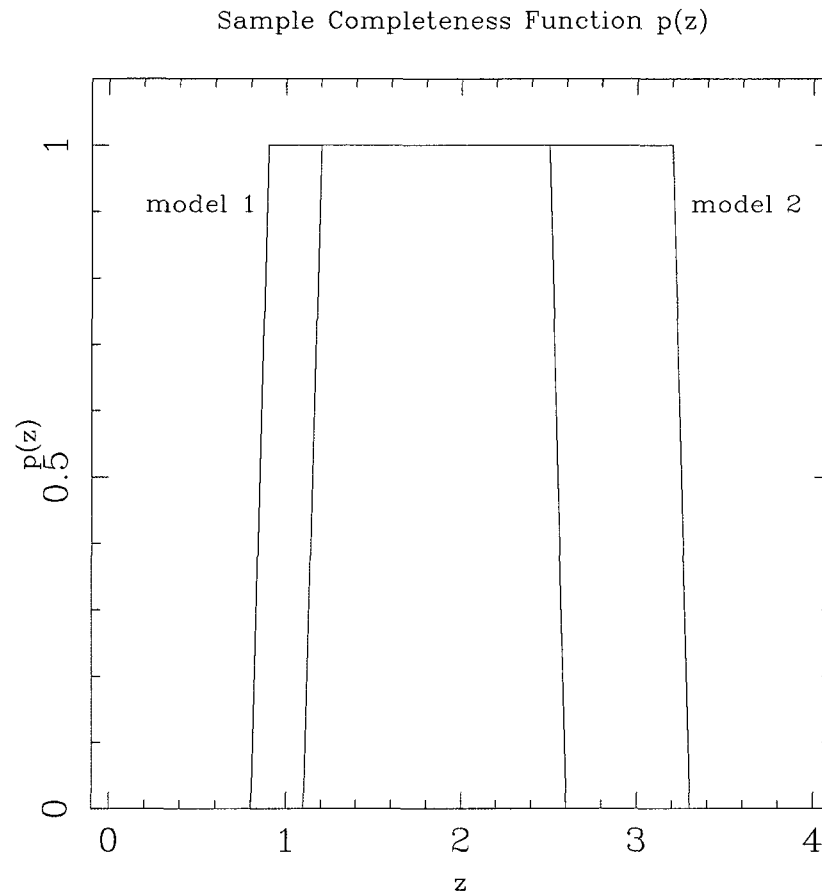


Figure 3.15: *Conceptual illustration of the probability box $p(z)$. Values of 1 are given to models that lie inside a specific locus in our color-color plots, for instance, redshifts of models for star-forming galaxy that lie left to the diagonal line will get a value of 1. Everything outside this region has a value of 0.*

After this procedure, we obtained a value for the effective volume for each different model shown in Figure 3.14. Figure 3.16 shows different values for effective volumes and how different models differ from each other. As can be seen, effective volumes for star-forming models do not change much for different $E(B-V)$ given a specific age but they do increase as the age of each model increases. To determine which value of effective volume will be adequate for our star-forming galaxies, we consider that a representative model for this population will be given by the blue line and asterisk symbol in Fig 3.16. This value represents a first approximation for an effective volume.

At redshift $z \sim 2$ the age of the universe is $\sim 3.2 \text{ Gyr}$ this is why we do not consider models older than this age, and it is unlikely that galaxies this old will be present at this redshift. We also discount models younger than $10^{7.28}$ years as the number of such galaxies must be small in any reasonable population. Our preferred V_{eff} is $2.06 \times 10^6 \text{ Mpc}^3/\text{deg}^2$, which corresponds to galaxies with age $10^{7.80}$ years. Our lower value is $1.47 \times 10^7 \text{ Mpc}^3/\text{deg}^2$ for galaxies with age $10^{7.28}$ years, And our upper value is $2.53 \times 10^7 \text{ Mpc}^3/\text{deg}^2$ for models with age $10^{9.36}$ years. Future work will include developing a better understanding of these models and the possible values of V_{eff} .

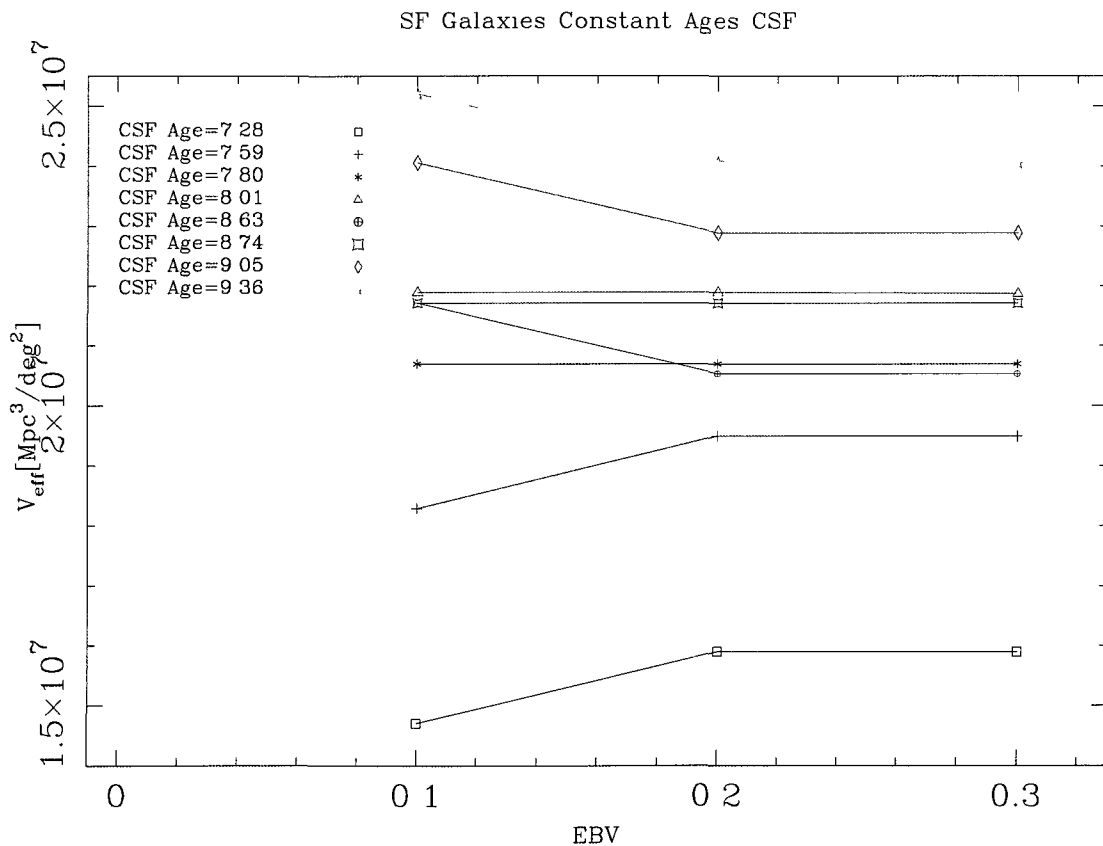


Figure 3.16: Effective volume as a function of $E(B-V)$ for different model ages. Different ages are represented by a continuous line of different colors, and each point represents a change in $E(B-V)$ within that model age. As can be seen V_{eff} does not change considerably with $E(B-V)$ but it does increase with age.

A similar analysis was developed for our passive galaxies. Figure 3.17 shows the different color

models in a gzK_s plot from spectral synthesis models: Ages range between 0.2 and 2 Gyr with $E(B-V)=0$. Different ages are represented with a different color and redshifts evolve as shown by the black arrow. Again, from this distribution of redshifts, only those that will lie inside the passive locus will have a probability $p(z)$ equal to one. Results of V_{eff} for every model are shown in Figure 3.18. As can be seen, V_{eff} can take a range of values for different ages, but it is possible that young galaxies will not be part of our sample (0.2 Gyrs). Most of our passive galaxies will consist of a sample of old galaxies. Also, it is possible that models with ages above 1.5 Gyr are too old, since most galaxies probably did not form at $z \sim 10$ but later. As a result, this V_{eff} value will only represent an upper limit.

Our preferred V_{eff} is $2.34 \times 10^7 \text{ Mpc}^3/\text{deg}^2$, which represents galaxies that formed at $z \sim 3$ and are being observed at $z \sim 2$ (age 1 Gyr). These 1 Gyr old galaxies have had enough time to evolve into a passive population. Our upper limit is $2.51 \times 10^7 \text{ Mpc}^3/\text{deg}^2$ which corresponds to an age of $10^{8.84}$ years and our lower limit is $1.14 \times 10^7 \text{ Mpc}^3/\text{deg}^2$ for an age $10^{9.36}$ years.

Now that we have a value of V_{eff} for star-forming and passive galaxies in our sample, using our galaxy number counts we can calculate our number density of galaxies using Equation 3.2

$$\phi_f(m) = 2 \frac{N_f(m)}{V_{\text{eff}}(m)}. \quad (3.2)$$

The factor 2 in Equation 3.2 converts between 0.5 magnitude bins to 1 magnitude bins.

3.2.2 Absolute Magnitudes

The final step in developing the luminosity function is to convert between apparent magnitudes $\phi(m)$ to absolute rest-frame R magnitudes $\phi(M)$. In the usual way, absolute magnitudes are calculated using the cosmological distance modulus DM and k-correction K to find the absolute magnitudes:

$$M_R = m_{\lambda_{\text{obs}}} - DM - K. \quad (3.3)$$

This expression can be re-written as:

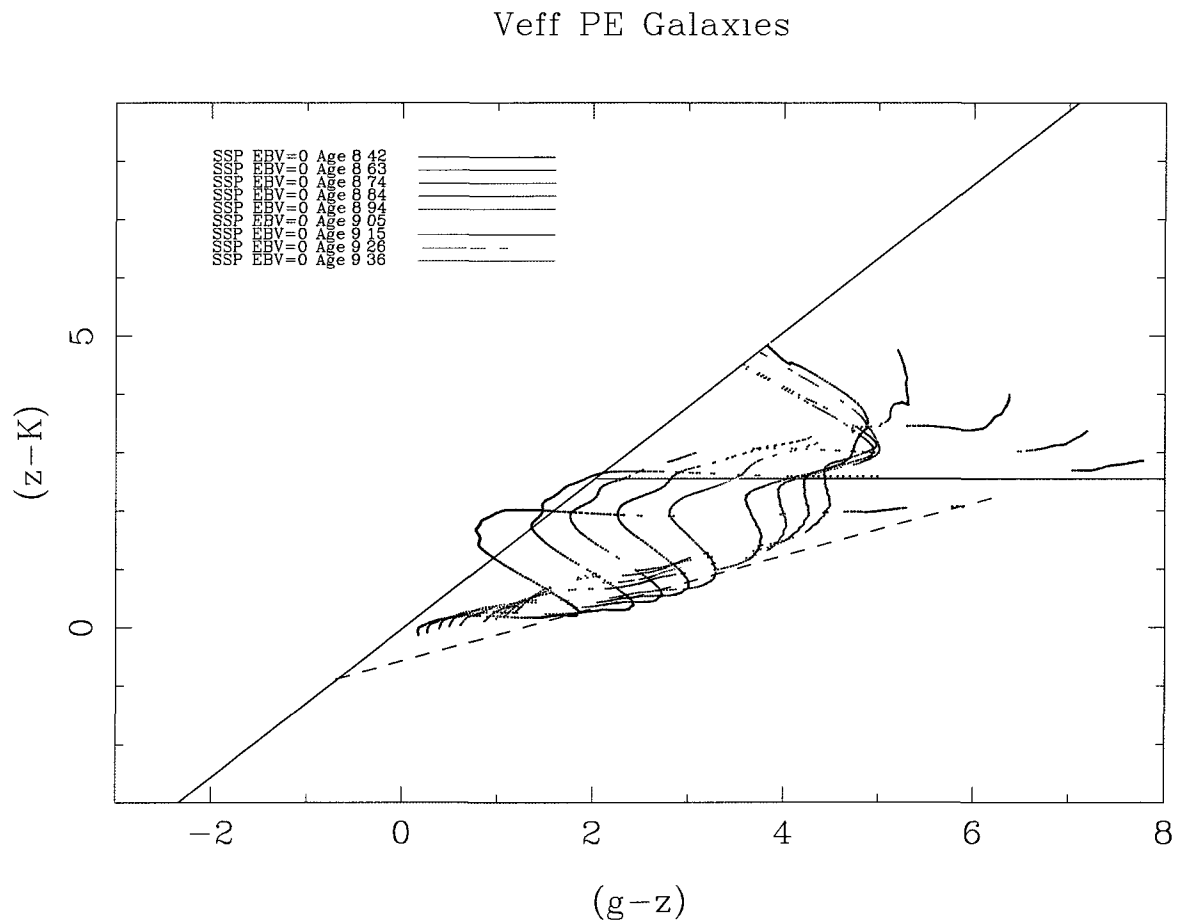


Figure 3.17: Color gzK_s Models from Bruzual & Charlot (1993) spectral synthesis models for passive galaxies. Ages range from 0.2 to 2 Gyr and $E(B-V)=0$. Each age is represented by a different color and only one possible $E(B-V)=0$

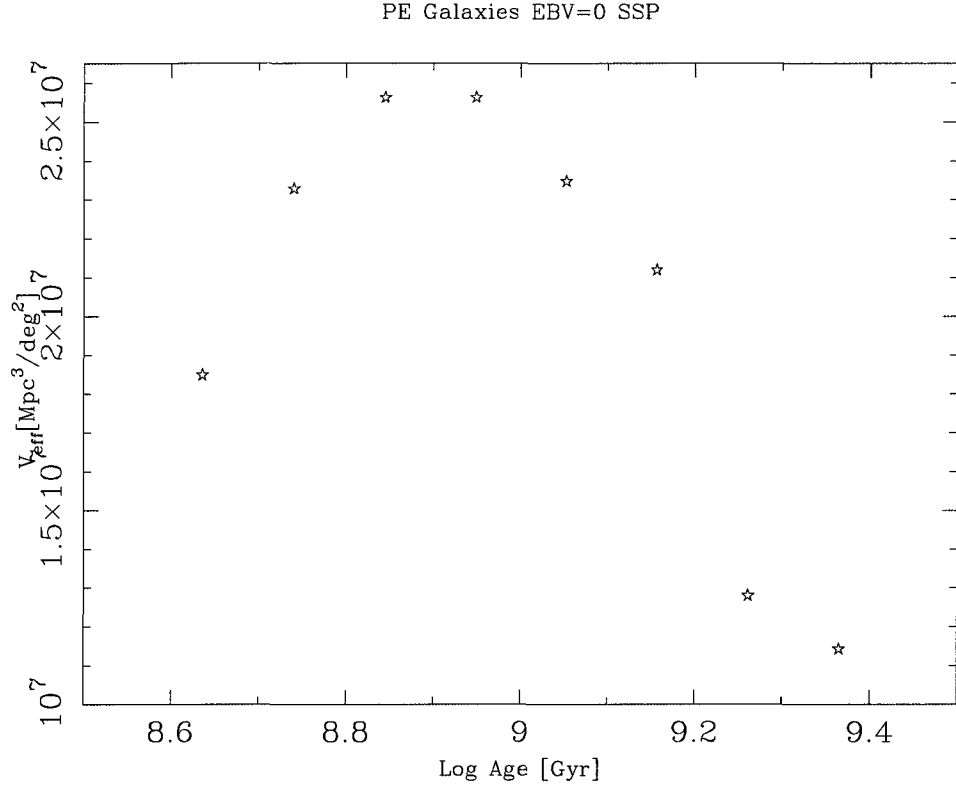


Figure 3.18: V_{eff} as a function of age for passive galaxies. Each point represents a different age and only one value of $E(B-V)=0$. Note that for models younger than $10^{8.94}$ we impose an upper redshift cutoff at $z = 4$.

$$M_R = m_{\lambda_{obs}} - 5 \log \left(\frac{D_L}{10 \text{ pc}} \right) + 2.5 \log(1+z) + \left(m_R - m_{obs\lambda_{(1+z)}} \right). \quad (3.4)$$

In Equation 3.4, D_L is the luminosity distance. The last term, $\left(m_R - m_{obs\lambda_{(1+z)}} \right)$, is the k-correction color between rest-frame R and the K_s filter which for galaxies at $z \sim 2$ will be very small due to our choice to work our luminosity function in rest-frame R.

To calculate absolute magnitudes we used SEDfit to obtain colors for stellar populations with constant star-formation and instantaneous burst models. From these color models we determined

ΔMag , the difference between the absolute rest-frame R magnitude and the observed K_s apparent magnitude. According to this, $\Delta\text{Mag}=(DM + K)$ will give us the correction to our apparent magnitudes needed to find the absolute magnitudes.

Figure 3.19 shows ΔMag as a function of redshift for several ages and dust models. Blue symbols are used to represent models for star-forming galaxies and red symbols are used for models of passive galaxies.

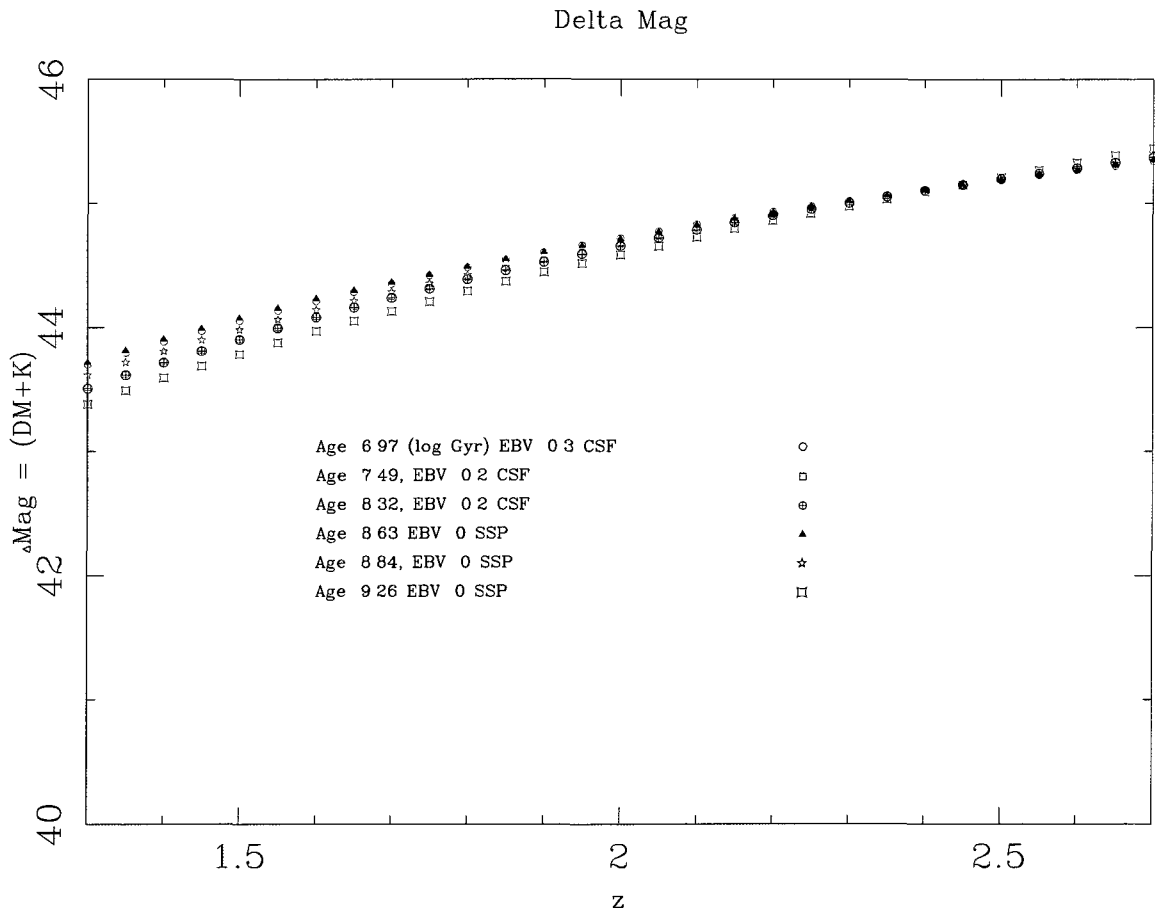


Figure 3.19: ΔMag as a function of redshift for several different models. Blue symbols are used to represent star-forming galaxy models and red symbols for models of passive galaxies.

Since our sample will have a redshift $z \sim 2$ we used the average value of the different models at this redshift (44.66). Since our models do have a range of values for ΔMag we consider these as an

upper and lower limit, which will be represented in our luminosity function as the magnitude of our error bars in M_R .

3.2.3 Rest-frame R Luminosity function for the CFHTLS Deep Fields

Results for our luminosity function in rest-frame R are shown in Figure 3.20, each Deep field is represented by a different symbol, circles for D1, stars for D2, triangles for D3 and squares for D4. Blue colors are used to identify galaxies that were selected as star-forming based on their $zJHK_s$ colors, while those galaxies that were classified as passive are represented with red. Filled circles are used to represent the average of the four Deep fields and their error bars are again an estimate of the scatter between the fields. Also shown, as solid blue and red lines in Figure 3.20, are the results of Hartley et al. (2008) luminosity functions for star-forming and passive galaxies.

As is reported in Hartley et al. (2008), star-forming galaxies seem to sample a wide range in luminosity. Moreover, as seen in the galaxy number counts for star-forming galaxies, there is a steep rise in the luminosity function for faint objects. Due to our choice to work in rest-frame R, our absolute magnitudes can be related to the mass of the galaxy, and as a result, the bright end of the luminosity function will represent the most massive systems. Compared with Hartley et al. (2008), we found a lower number density of $z \sim 2$ star-forming galaxies. This difference is too large to be due to differences in cosmic variance. There are two possible explanations for this fact, one could be due to differences in volume estimates and the second could be due to McCracken et al. (2010) observation implying that there is a mistake in Hartley et al. (2008) transformations to the Daddi et al. (2004) system.

As observed for our passive galaxy number counts, our luminosity function for passive galaxies shows a flattening at the faint end and a possible turnover. This would imply that the passive galaxy population at this epoch will be dominated by bright (massive) objects. This phenomenon is consistent with the “downsizing” scenario. Downsizing as introduced by Cowie et al. (1996), implies that star-formation stops in massive systems first and in low mass systems later. Our observations are consistent with the downsizing scenario: if we interpret rest-frame R-band luminosity

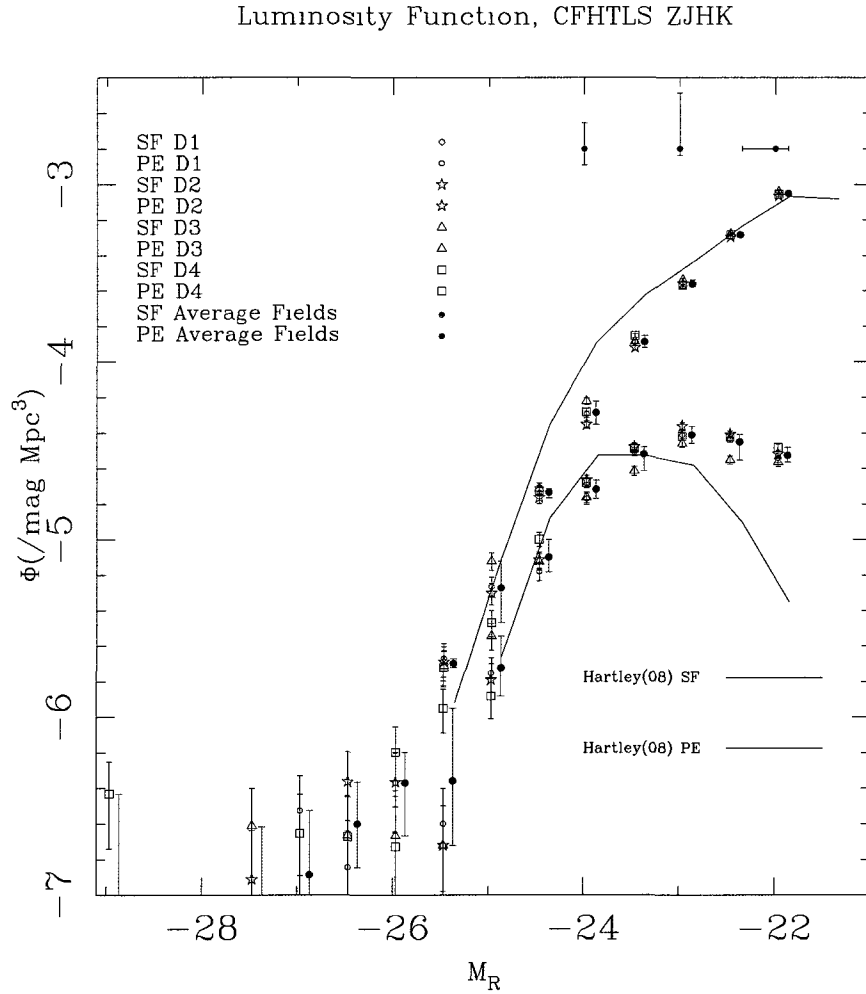


Figure 3.20: Redshift $z \sim 2$ R band luminosity function for the four Deep fields of the CFHTLS. Blue symbols represent galaxies that were classified as star-forming based on their $zJHK_s$ colors, red symbols represent passive galaxies classified under the same color-selection. Each Deep field is represented with a different symbol, as indicated in the figure. For comparison we show the luminosity function of Hartley et al. (2008) for star-forming and passive galaxies as blue and red solid lines. Blue and orange filled circles represent the average luminosity function for star-forming and passive galaxies for our four fields. Error bars for individual fields are \sqrt{N} , while the error bars for the average fields is an estimate of the scatter between fields. Points have been shifted horizontally from the bin mid-point for clarity. In the upper part of the figure, the horizontal error bar is an estimate between our best guess in absolute magnitude and the difference between this best guess and our upper and lower limits. Vertical blue and red error bars are also an estimate of how our luminosity function will change taking into account our upper and lower limits of V_{eff} .

as a surrogate for the stellar mass of a galaxy, then at the low mass end most galaxies are still star forming, while at the massive end approximately one in three to one in four galaxies are passive. Our results at the faint end are higher than Hartley et al. (2008), as was explained before, this difference could be due to differences in V_{eff} or by incorrect transformations to the Daddi et al. (2004) system from Hartley et al. (2008) (McCracken et al. 2010).

It is important to notice that flattening and a turnover in the luminosity function are consistent with downsizing. Nevertheless, a turnover will represent a much more interesting scenario because there is a magnitude (mass) in which galaxies are more likely to evolve into passive systems. This could hold some kind of connection to the galaxy's feedback processes.

Chapter 4

Summary, Conclusions and Future Directions.

The BzK_s selection criteria is the most complete method to select and distinguish galaxies at $z \sim 2$ based only color-color cuts from three different broad band filters. It provides the opportunity to study galaxy evolution in specific populations (passive and star-forming) to obtain a more complete picture in the exploration of these different populations. This technique, combined with the large effective areas ($0.4\text{-}1 \text{ deg}^2$) and independent lines of sight of the four Deep Fields in the Canada France Hawaii Telescope Legacy Survey, allowed us to construct a representative sample of star-forming and passive galaxies. In order to do so, we constructed a new gzK_s selection criteria to match the BzK_s technique to the available CFHTLS filters, and then, to address incompleteness in our sample due to non-detections in g-band we developed and applied a second color selection based on the $zJHK_s$ filters. This procedure allowed us to obtain a statistical analysis of galaxies at this important redshift ~ 2 .

Our main findings are:

1. Our results in galaxy number counts seem to be in good agreement with most authors (Kong

et al. (2006) and McCracken et al. (2010)). For star-forming galaxies, our results are significantly lower than those obtained by Lane et al. (2007) and Hartley et al. (2008). Lane et al. (2007) attributed the difference between their number counts of star-forming galaxies with previous results by Kong et al. (2006) to cosmic variance. Comparing our scatter between our four different fields, cosmic variance does represent a slight change in our number counts, but does not seem to account for such a large difference as to match Lane et al. (2007) number counts.

2. Galaxy number counts for passive galaxies seem also to be in good agreement with most authors but seem to be higher than those of Hartley et al. (2008). Nevertheless, this difference seems to be attributed to an incorrect transformation to the Daddi et al. (2004) system by Hartley et al. (2008) (McCracken et al. (2010)). Our galaxy number counts for passive galaxies exhibit a flattening at faint magnitudes and -in some fields- a possible turnover as observed previously by McCracken et al. (2010) in their single field. This variation between our four fields could imply that this turnover is not universal.
3. Our rest-frame R-band Luminosity function for star-forming galaxies samples a wide range in luminosities which can be related to the mass of the galaxy, due to our choice to work with rest-frame R-band. The luminosity function for passive galaxies exhibits a flattening and a possible turnover. This feature is an indication of “downsizing” scenario, in which the most massive galaxies (bright end of the luminosity function) shut down star-formation before the less massive systems (faint end of the luminosity function). This is why there is a large fraction of faint (low mass) star-forming galaxies while at the massive end a much smaller fraction is star-forming. A possible turnover in the luminosity function for passive galaxies is an interesting feature that could raise many questions as to why this specific mass (magnitude) is more effective at shutting off star-formation in galaxies, and whether or not this scenario is related to processes of galaxy feedback.

4. One of the main advantages in working with the four Deep Fields available at the Canada France Hawaii Telescope Legacy Survey is that they provide four large independent effective areas, which allows us to make some estimates on cosmic variance. As can be observed, in this large fields, cosmic variance seems to be small but is not negligible for galaxies at $z \sim 2$. Nevertheless, it is still necessary to construct a better estimate of cosmic variance in our fields.

4.1 Future Work

Several features are necessary to improve our results. For example, our completeness corrections need to be calculated for our remaining fields (D2, D3 and D4). Also our estimates in the effective volume V_{eff} for our luminosity functions represents a first approximation, and further work is necessary to construct a better value for V_{eff} . By considering a probability function $p(z)$ that includes an estimate of the photometric scatter between the regions of our color-color plot. A good estimate of cosmic variance could be obtained by exploring a large number of independent fields in the sky, but this could require additional observations. A less expensive approach to this limitation is to construct an estimate in cosmic variance based on bootstrapping, or resampling our data by random drawing of our data. Finally, it is also necessary to obtain a conversion between K_s magnitude and galaxy mass to describe this results in terms of mass (Construct a Mass Function).

Bibliography

- [1] Bruzual G., Charlot S., 1993, ApJ 405, 538.
- [2] Bruzual G., Charlot S., 2003, MNRAS 344, 1000.
- [3] Calzetti D., Armus L., Bohlin R.C., et al. 2000, ApJ 533, 682.
- [4] Cimatti A., et al. 2002, A&A 381, L68.
- [5] Cimatti A., 2003. RMxAC 17, 209.
- [6] Cimatti A., 2004, Ap&SS.294:23.
- [7] Cowie L, Songaila A., Hu M., et al. 1996, AJ 112, 3.
- [8] Daddi E., Cimatti A., Renzini A., et al., 2004, ApJ 600, 127.
- [9] Daddi E., Cimatti A., Renzini A., et al., 2004, ApJ 617, 746.
- [10] Dunne L., Ivison, R.J., Maddox S., et al. 2009, MNRAS 390, 3.
- [11] Franx M., Labbé I., Rudnick G., et al. 2003, ApJ 587, L79.
- [12] Glazebrook and Economou 1997, The Perl Journal, 5,5.
- [13] Grazian A., Salimbeni, S., Pentericci L., et al., A&A 465, 393.
- [14] Hartley W.G., Lane K.P., Almaini O., et al. 2008, MNRAS 391, 1301.

- [15] Kong X., Daddi E., Arimoto N., et al. 2006, ApJ 638, 72.
- [16] Kron R., 1980, ApJS, 43, 305.
- [17] Lane K., Almaini O., Foucaud S., et al. 2007, MNRAS 379, L25.
- [18] McCracken H.J., Capak, P., Salvato, M., et al. 2010, ApJ 708, 202.
- [19] Messias H., Afonso J., Hopkins A., et al. 2010, ApJ 719, 790.
- [20] Reddy N., Erb D., Steidel C., et al. 2005, ApJ 633, 748.
- [21] Sawicki M., 2011, MNRAS, submitted.
- [22] Sawicki M., Thompson D., 2006, ApJ, 642, 653.
- [23] Schlegel D., Finkbeiner D., Davis M., 1998, ApJ, 500, 525.
- [24] Steidel C.C., Shapley A., Pettini M., et al., 2009 ApJ 604, 534.
- [25] van Dokkum P., Franx, M., Förster Schreiber N., et al. 2004, ApJ 611, 703.
- [26] CFHT MegaCam, *Technical considerations to prepare MegaCam observations*, <http://www.cfht.hawaii.edu/Instruments/Imaging/MegaPrime/specsinformation.html>, recovered June 20, 2011.
- [27] Mega Prime, CFHT MegaCam Legacy Survey, *CFHTLS Deep & Wide Fields*, <http://www.cfht.hawaii.edu/Science/CFHLS/cfhtlsdeepwidefields.html>, recovered June 12, 2011.
- [28] The Canadian Astronomy Data Centre, *The MegaCam ugriz filter set*, <http://cadwww.dao.nrc.ca/megapipeline/docs/filters.html>, recovered March 18, 2011.
- [29] Canada-France-Hawaii Telescope, *WIRCam Filters*, <http://www.cfht.hawaii.edu/Instruments/Instruments/Wircam.html>, recovered March 18, 2011.

- [30] Canada-France-Hawaii Telescope, *Technical considerations to prepare MegaCam observations*, <http://cfht.hawaii.edu/Instruments/Imaging/Megacam/specsinformation.html> , recovered June, 2011.
- [31] E. Bertin, *SExtractor v2.5 User's Manual*, Institut d'Astrophysique and Observatoire de Paris, 2006.
- [32] INAF Osservatorio Astrofisico di Arcetri *K20 Survey*, Institut d'Astrophysique and Observatoire de Paris, 2006, <http://www.arcetri.astro.it/k20/releases>, recovered August 3, 2011.



**Saint Mary's
University**

Halifax, Nova Scotia
Canada B3H 3C3

Patrick Power Library

tel 902.420 5534

fax 902 420.5561

web www.stmarys.ca

Copyright Permission Notice

Documentation regarding permissions for the use of copyrighted material in this thesis is on file at the Saint Mary's University Archives. Contact us if you wish to view this documentation:

Saint Mary's University, Archives
Patrick Power Library
Halifax, NS
B3H 3C3

Email: archives@smu.ca

Phone: 902-420-5508

Fax: 902-420-5561